# A Morphodynamic Modeling Study on the Formation of the Large-Scale Radial Sand Ridges in the Southern Yellow Sea

Tao, Jianfeng; Wang, Zhengbing ; Zhou, Zeng; Xu, Fan; Zhang, Changkuan; Stive, Marcel

**DOI**
10.1029/2018JF004866

**Publication date**
2019

**Document Version**
Final published version

**Published in**
Journal of Geophysical Research: Earth Surface

JGR Earth Surface

RESEARCH ARTICLE
10.1029/2018JF004866

# A Morphodynamic Modeling Study on the Formation of the Large-Scale Radial Sand Ridges in the Southern Yellow Sea

**Jianfeng Tao[1,2,3], Zheng Bing Wang[2,3,4], Zeng Zhou[2,5], Fan Xu[2,5,6], Changkuan Zhang[2], and Marcel J.F. Stive[3]**

[1]State Key Laboratory of Hydrology-Water Resources and Hydraulic Engineering, Hohai University, Nanjing, China, [2]College of Harbor, Coastal and Offshore Engineering, Hohai University, Nanjing, China, [3]Faculty of Civil Engineering and Geosciences, Delft University of Technology, Delft, The Netherlands, [4]Deltares, Delft, The Netherlands, [5]School of Environment, The University of Auckland, Auckland, New Zealand, [6]State Key Laboratory of Estuarine and Coastal Research, East China Normal University, Shanghai, China

**Key Points:**
- The unique giant fan-shaped morphology of the radial sand ridges (RSRs) is numerically simulated
- The formation of the RSRs requires delicate conditions governed by currents originating from the rotational, progressive tidal wave system
- The mechanism underlying the asymmetric spatial pattern of the RSRs is revealed

**Supporting Information:**
- Supporting Information S1

**Correspondence to:**
Z. Zhou and F. Xu,
zeng.zhou@hhu.edu.cn;
fxu@sklec.ecnu.edu.cn

**Citation:**
Tao, J., Wang, Z. B., Zhou, Z., Xu, F., Zhang, C., & Stive, M. J. F. (2019). A morphodynamic modeling study on the formation of the large-scale radial sand ridges in the Southern Yellow Sea. *Journal of Geophysical Research: Earth Surface*, *124*, 1742–1761. https://doi.org/10.1029/2018JF004866

Received 6 SEP 2018
Accepted 10 JUN 2019
Accepted article online 20 JUN 2019
Published online 5 JUL 2019



**Abstract** The radial sand ridges (denoted as "RSRs" hereafter) in the Southern Yellow Sea, China, are morphologically striking because of the remarkable size and radial planar orientation, standing out as a unique coastal geomorphology among the worldwide sand ridge systems. The formation of this giant fan-shaped geomorphic feature requires delicate conditions and awaits in-depth investigation. Using an idealized morphodynamic model, this study unravels the governing factors for the formation of the unique large-scale RSRs, in comparison with other types of sand ridge systems over the world. The effects of the $M_2$ tidal constituent, the Coriolis forcing, the bed resistance, and the initial water depths on the morphodynamic behavior of the RSRs are explored. Numerical results indicate that the tidal regime, characterized by rotational and progressive current action associated with the tidal bulge, is dependent on the eastern coastline of China as well as latitudinal effects. Through the comparison between the simulated and the measured morphology, this tidal regime is demonstrated to be the key driver in forming and maintaining the present-day RSRs. The runs with different parameters further suggest that the asymmetric pattern of the RSRs, which shows larger northern sand ridges than the southern ones, results from both the asymmetric distribution of current activity caused by the tidal bulge and unequal sediment supply. Overall, this study highlights the delicate condition, predominantly represented by the particular currents set up by the tidal wave system and the sediment supply, required to shape the striking large-scale RSRs in the Southern Yellow Sea.

## 1. Introduction

Sand ridges are geomorphic features widely distributed in estuaries (e.g., the Thames Estuary; Harris, 1988), coastal bays (e.g., the Gulf of Korea; Off, 1963), the ends of straits (e.g., the Dover Straits; Caston, 1981), and continental shelves (e.g., the North Sea and the East China Sea; Belderson et al., 1982; Stride, 1982; Yang, 1989). The formation of sand ridges favors an environment where abundant sediment is available and the hydrodynamic regime is sufficiently strong to transport sediments (Dyer & Huntley, 1999; Liu & Xia, 1985; Off, 1963; Pattiaratchi & Collins, 1987; Swift, 1975). Most sand ridges around the world are hidden subaqueous landscapes characterized by striking and intricate morphologies, which have received considerable Holocene shelf deposits and/or fluvial sediment supply. These sediments are subsequently reworked by both terrestrial and marine processes, including river inflows (Giosan et al., 2005), wind waves (Hulscher et al., 1993), tidal currents (Van de Meene & Van Rijn, 2000a, 2000b), and storm surges (Calvete et al., 2001; Swift, 1975; Trowbridge, 1995).

Sand ridges typically exhibit horizontal length scales ranging from several kilometers (mostly in estuaries or river deltas) to hundreds of kilometers (generally on continental shelves) and are characterized by a "wavelength" of several kilometers and an interridge depth of tens of meters (Gao & Collins, 2014). In most cases, the crests of sand ridges are parallel or subparallel to the main tidal current direction (Dyer & Huntley, 1999; Gao & Collins, 2014; Liu & Xia, 1985). At the end of straits or coastal bays where flow diverges or converges, sand ridges often show a fingered or radial planar pattern, such as the sand ridges observed at the Dover Straits (Caston, 1981) and the Southern Yellow Sea (Liu et al., 1989).

Off (1963) was probably the first to define sand ridges as rhythmic linear sand bodies induced by tidal currents. Since then, the geomorphic characteristics and the dynamics of sand ridges have attracted a considerable research effort over the last 50 years, particularly on the tidal shelf seas around the UK and on sand ridges in the North Sea and the Atlantic coast of North America (Caston, 1981; Collins et al., 1995; Dyer & Huntley, 1999; Houbolt, 1968; McBride & Moslow, 1991; Swift, 1975). Attention has been given to fundamental theories for the formation and long-term evolution of sand ridges, so that quantitative geomorphic prediction of sand ridges can be modeled (Dyer & Huntley, 1999). Huthnance (1982a) first derived theoretical relationships that predict the wavelength and the orientation of tidal sand ridges. These relationships are supported by the field data from the Norfolk Sandbanks. Huthnance (1982b) further explained that the refraction of tidal currents over a sand ridge could generate a residual flow, which resulted in the convergence of sediment toward the crest of the sand ridge. This theory was further extended to explain other bed forms, such as shoreface-connected ridges (Calvete et al., 2001; Trowbridge, 1995; Walgreen et al., 2002), linear sand ridges (De Vriend, 1990), and long bed waves (Blondeaux et al., 2009).

Recent advances on long-term morphodynamics by solving the nonlinear governing equations numerically (Lesser et al., 2004; Roelvink, 2006; Wang et al., 1995) allow us to simulate the morphodynamic evolution of a system and hence to gain fundamental insights into the ontogeny of coastal landscapes (Zhou, Olabarrieta, et al., 2014; Zhou et al., 2017). Hibma et al. (2003, 2004) simulated the formation of finite-amplitude tidal sand bars in a long straight tidal basin. Marciano et al. (2005) investigated the channel-shoal patterns in a short tidal basin with both theoretical stability analysis and numerical modeling. These studies indicated that the simulated morphologies are affected by the initial bathymetry, the Shields parameter, and the sediment supply. Moreover, the Coriolis force has also been found to pronouncedly affect the channel-shoal patterns in estuaries (Schramkowski & De Swart, 2002; Van Leeuwen & De Swart, 2002).

The largest sand ridge system along the Chinese coast (Wang, Zhang, et al., 2012), the radial sand ridges (hereafter referred to as "RSRs") in the Southern Yellow Sea, is morphologically striking because of the remarkable size and radial planar orientation (Figures 1a and 1b). These huge sand bodies are habitats to a variety of species and provide potential land resources and ideal locations for deep-water harbors. The unique features, environmental functions, and socioeconomic values of the RSRs raised interesting questions concerning their morphodynamics. Many researchers attempted to answer the question why are they there? What are the relevant and necessary conditions for the formation/presence of the RSRs? It has been suggested that the RSRs originated from the underlying Holocene strata relict (Li et al., 2001; Wang et al., 1999; Wang, Zhang, et al., 2012; Yang, 1989) with sediments coming from the neighboring Yangtze River and the Yellow River (Lee & Chough, 1989; Milliman & Meade, 1983; Saito & Yang, 1994). The Jiangsu coastline has advanced seaward about 20–40 km over the last one thousand years, because of the abundant sediment supply (Wang, Zhang, et al., 2012; Zhang, 1984). After the Yellow River diverted from the Yellow Sea into the Bohai Sea in 1855, part of the sediments of the Old Yellow River Delta were reworked and reformed into the RSRs (Zhou, Liu, et al., 2014), which in turn provided natural shelters for the tidal flats behind the offshore sand ridges.

Although originating in an earlier environment, sand ridges are dynamic systems which are undergoing modification in response to their present environment, especially the hydraulic regime (Dyer & Huntley, 1999). Many studies have been conducted attempting to elucidate the mechanism underlying the formation of the present-day RSRs (e.g., Du & Wang, 2014; Zhang et al., 1999; Zhu & Chang, 2001). The offshore tidal regime along the Jiangsu Coast has been recognized as the key driving force shaping the RSRs, which is supported by two observations: (1) Both the tidal current fields and the morphology of the RSRs show similarly radial spatial patterns (e.g., Ren, 1986; Zhang, 2012; Zhang et al., 1999), and (2) several authors found that the radial tidal current patterns can be modeled in the absence of the RSRs (e.g., Qian et al., 2015; Xu et al., 2016; Zhu & Chang, 2001; Zhu & Chen, 2005). The radial tidal current fields are governed by the convergence of a progressive tidal bulge from the East China Sea and a local reflected tidal "wave" formed by the obstruction of the Shandong Peninsula (Zhang et al., 1999; see also Qian et al., 2015; Xu et al., 2016). Other dynamics, such as waves (Xiong et al., 2017) and storm surges (Ren et al., 1985), are considered to be less relevant to the radial morphology of the RSRs, although they can induce considerable short-term sediment transport.

The $M_2$ tidal constituent is dominant in the RSRs (Ren, 1986; Uehara et al., 2002; Zhang, 2012), which has been considered as the major tidal forcing shaping the present-day RSRs (Xing et al., 2012; Xu et al., 2016;

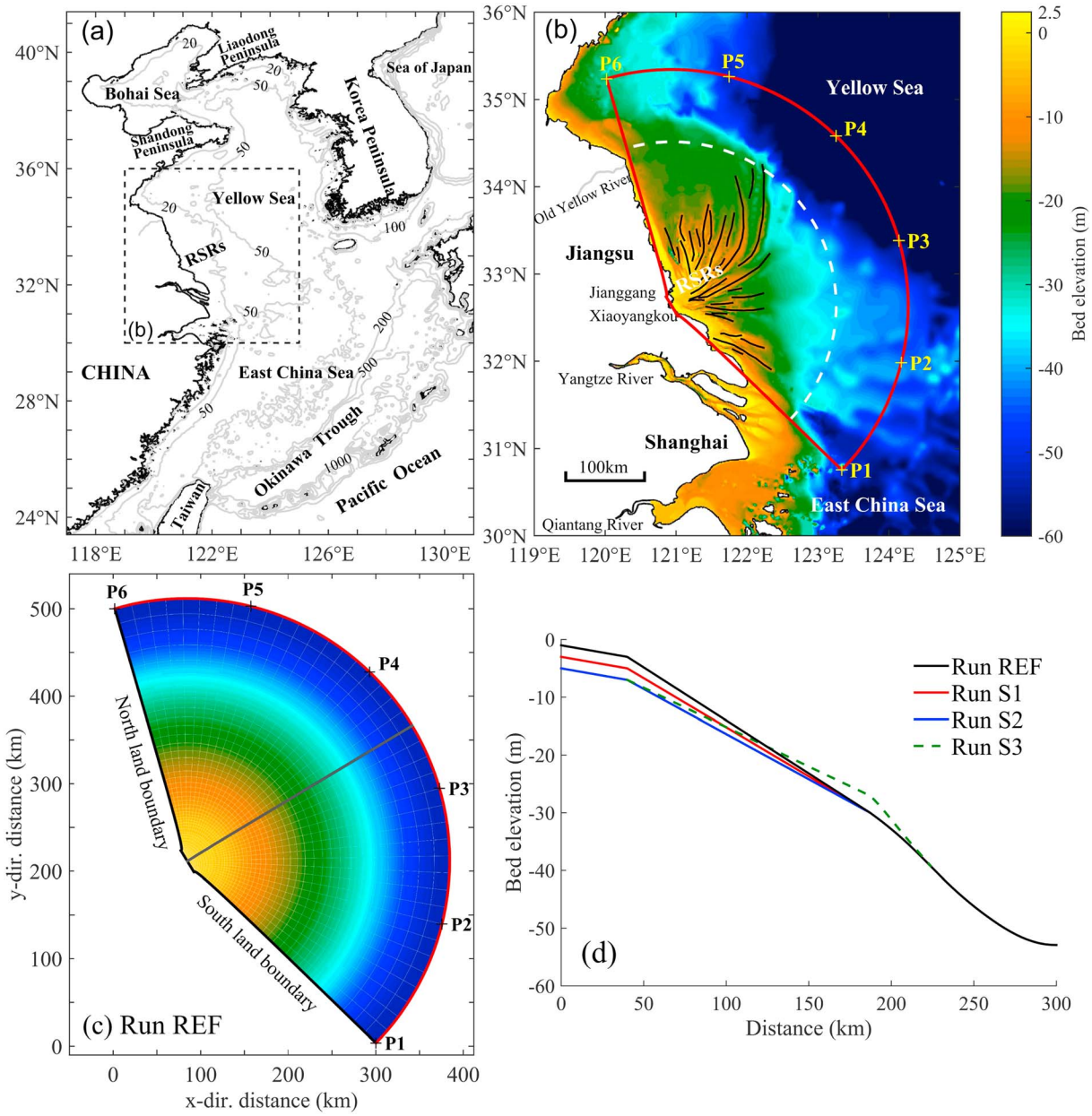


**Figure 1.** Regional settings of the study area and schematized model configurations. (a) Bathymetry of the Bohai Sea, the Yellow Sea, and the East China Sea. The bathymetric data are after the gridded bathymetry data of General Bathymetric Chart of the Oceans with 30-arc sec interval grid; bathymetry contours are given in meters. (b) Bathymetry of the Southern Yellow Sea and the East China Sea. Location indicated by the black dashed box in (a). Bathymetric data were measured in 2006. The black lines roughly denote the sand ridges in RSRs system. The white dash sector covers the area of the RSRs and is also the area of geomorphic change in simulation scenarios. The red lines indicate the schematized model geometry used in this study. The cross markers (P1 to P6) show the nodes for prescribing tidal level along the boundary. (c) Plan view of the geometry, grid, and bathymetry of the schematized model. The color bar in (c) is the same as that of (b). (d) Longitudinal profiles of the bathymetry with different initial bed levels. Location of the longitudinal profile is indicated by the gray line in (c). The bed elevation is relative to mean sea level. RSRs = radial sand ridges.

Zhang et al., 1999). Previous conclusions about the formation of the RSRs were mainly based on the short-term tidal current fields and the analyses from classical theoretical studies (e.g., Huthnance, 1982a; Off, 1963; Zhang et al., 1999; Zhu & Chang, 2001). Although these indirect proofs are reasonable, a direct evidence lacks to demonstrate the causal relationship between the tidal regime and the unique planimetric shape of the RSRs that differ from other sand ridges worldwide. In this study, a state-of-the-art morphodynamic model (Delft3D) is employed to investigate the formation of the RSRs. It is worth noting that this study does not aim to reproduce the exact morphology of the RSRs. We restrict the

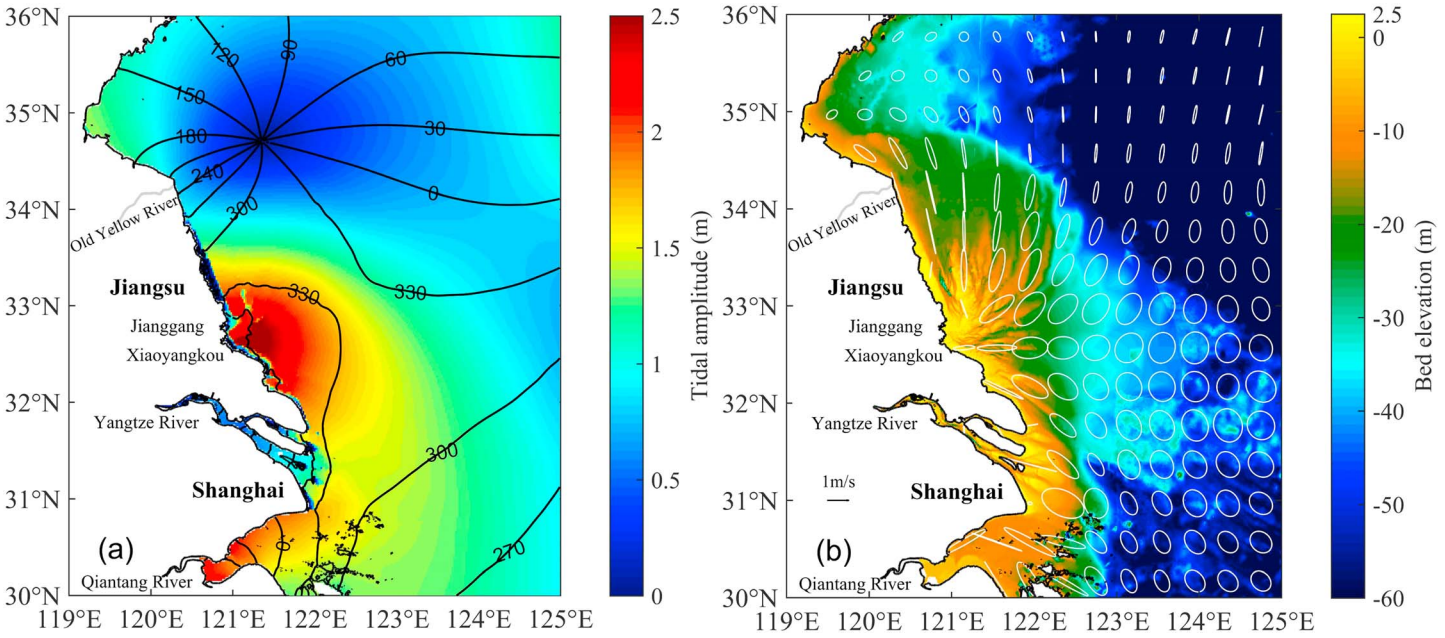


**Figure 2.** (a) Cotidal chart and (b) tidal current ellipses of the $M_2$ constituent in the Southern Yellow Sea (modified after Tao et al., 2018). The color code in (a) indicates tidal amplitudes with black cophase lines in degrees. The color code in (b) shows the bed elevation of the Southern Yellow Sea.

research questions to the following: (1) Whether the dominant $M_2$ tidal constituent can shape the radial planimetric shape of the RSRs or not? (2) How do tidal regime and sediment supply affect the spatial pattern of the RSRs? By resolving these two questions, we intend to gain a more in-depth understanding of the mechanisms underlying the morphodynamics of the RSRs. This morphodynamic study also aims to facilitate further research effort to predict the long-term evolution of the RSRs under threats of sea-level rise, reduced sediment supply, and increased frequency of coastal storms.

## 2. Study Area

The RSRs off the Jiangsu Coast spread on the seabed on the western margin of the Pacific Ocean, where the long, gentle slope of the coastal plains extends offshore toward the semienclosed Yellow Sea (Figure 1a). The subaqueous sand ridges stretch more than 200 km from north to south and approximately 140 km from east to west, showing an approximately 150° fan-shaped spatial pattern centered on Jianggang (Xu et al., 2016). The plane scale of each sand ridge is up to 100 km long and 5–10 km wide (Liu et al., 1989), and the water depth in tidal channels can reach 30 m (Wang, Zhang, et al., 2012). The spatial pattern of the RSRs is asymmetric characterized by northern sand ridges larger than the southern ones (Xu et al., 2016). The bottom sediment of the RSRs mainly consists of fine to very fine sand, with a mean grain size of 62.5–250 μm (Liu et al., 1989; Wang & Ke, 1997), and the sediment mixture is well-sorted (Liu et al., 2012).

The hydrodynamics over the RSRs are characterized by astronomical tidal movements and wind waves. The tide over the sea area of the RSRs is semidiurnal with a mean tidal range of 4–6 m (Zhang et al., 1999). The tidal currents tend to be radial in a planar pattern and strong in magnitude, with measured maximum tidal current velocity up to 2.5 m/s (Wang, Zhang, et al., 2012). Under normal conditions, wave energy progressively decreases when crossing the RSRs so that wave heights of 7–9 m in the open sea are reduced to approximately 0.4 m at the coast. Under extreme wind conditions, although wave heights of 2 m can are occasionally observed, the probability is only 5% (Wang, Zhang, et al., 2012). According to the meteorological record from 1949 to 2007, only 5 of the 76 typhoons landed on the Jiangsu Coast or the Yangtze Estuary (Xu et al., 2016).

Figure 2 shows the cotidal chart and tidal current ellipses of the $M_2$ constituent. The area of the RSRs is influenced by two tidal systems, including the progressive tidal-bulge migration from the East China Sea and the anticlockwise rotation characterized by an amphidromic point approximately 220 km north of Jianggang (Figure 2a). These two tidal systems converge along the Jiangsu Coast, resulting in an approximately

stationary tidal wave, of which the phase difference between the current velocity and tidal level is about 90° over the central RSRs (Li et al., 2001; Tao et al., 2018; Xu et al., 2016; Zhang et al., 1999). Both the magnitudes of the current velocities and the tidal amplitudes peak in the central RSRs, due to the convergence of the two tidal systems. The tidal current fields in the RSRs show a radial in planar pattern centered in Jianggang (Figure 2b), which is consistent with the fan-shaped morphology of the RSRs (e.g., Tao et al., 2018; Xu et al., 2016). The tidal current ellipses show a bidirectional flow in the north and a rotational flow in the south over the RSRs.

## 3. Methodology

### 3.1. Numerical Model

An open-source morphodynamic model (Delft3D) is employed in the present study (Lesser et al., 2004). Since the model has been described in detail elsewhere (e.g., Van der Wegen & Roelvink, 2008), the governing equations are not introduced herein. The numerical model solves the nonlinear 2-D shallow water equations resulting in a detailed description of the flow field (i.e., water levels and velocities) over the model domain. The water level and the velocity fields are then utilized to calculate the sediment transport and the resultant bed evolution.

The sediment transport rate is calculated based on the local instantaneous flow condition using the widely adopted formula of Engelund and Hansen (1967), which accounts for both bed load and suspended load (following, e.g., Marciano et al., 2005; Van der Wegen & Roelvink, 2008; Van Maanen et al., 2013):

$$S = \frac{0.05U^5}{\sqrt{g}C^3\Delta^2 D_{50}}, \tag{1}$$

where $S$ is the total volumetric sediment transport flux, per unit of length ($m^3/ms$), $U$ is the magnitude of depth-average flow velocity (m/s), $g$ is the acceleration of gravity ($m/s^2$), $C = H^{1/6}/n$ is the Chézy friction coefficient ($m^{1/2}/s$), $H$ is the water depth (m), $n$ is the Manning coefficient ($s/m^{1/3}$), $\Delta$ is the relative density $(\rho_s - \rho_w)/\rho_w$, $\rho_s$ is the sediment density ($kg/m^3$), $\rho_w$ is the water density ($kg/m^3$), and $D_{50}$ is the median grain size (m). Effects of longitudinal and transversal bed slope on the sediment transport are accounted for following Bagnold (1966) and Van Rijn (1993) as described in detail by Van der Wegen and Roelvink (2008). The elevation of the bed is dynamically updated linearly by a geomorphic factor at each hydrodynamic time step according to mass conservation of sediment (Roelvink, 2006).

### 3.2. Numerical Experiments

The computational domain is idealized on the basis of the east coast of China, such that the physical implications of different factors can be analyzed in a more straightforward manner (Figure 1b). The embayment is a fan-shaped area of approximately 150° open angle. The center of the embayment is a 30-km-long line segment, which approximates the distance between Jianggang and Xiaoyangkou (Figure 1b). The lengths of the two lateral closed boundaries are both 300 km. The embayment is discretized using an orthogonal curvilinear grid with 200 × 220 cells (Figure 1c). The sizes of the grid cells range from 150 × 200 $m^2$ at the landward segment to 3.5 × 4 $km^2$ along the seaward arc boundary for the consideration of the balance between the numerical precision and efficiency. The computational time to perform each long-term simulation (up to 2,000 years) is approximately 2 weeks using a 3.7-GHz processor, 8.0 GB RAM personal computer.

A reference run (denoted as "REF" hereafter) is designed to reproduce the typical tidal system over the RSRs. The tidal amplitudes and the phases of the $M_2$ constituent at points P1–P6 along the seaward boundary are provided by a well-calibrated large-scale tidal numerical model that uses realistic shoreline and bathymetry (Tao et al., 2009). Other main semidiurnal tidal constituents (e.g., $S_2$, $N_2$, and $K_2$) can produce similar tidal regime but less significant tidal amplitudes or current velocities. Diurnal tidal constituents (e.g., $K_1$, $P_1$, $O_1$, and $Q_1$) do not result in the convergence to the central area or radial tidal current fields (Song et al., 2013; Tao et al., 2009). Therefore, these components are not considered for the ease of analysis (e.g., Ren, 1986; Uehara et al., 2002; Zhang, 2012). The Coriolis force is calculated based on realistic latitude spatially varying from 30.7°N to 35.2°N (Figure 1b). The initial water depths are set increasing radially from the central landward segment to the seaward boundary (Figure 1c). The radial profile consists of a linear sloping upper-flat segment (0.05‰; Wang, Gao, et al., 2012), a relatively steep lower-flat one (0.18‰; Wang & Ke, 1997), and a

**Table 1**
*Model Configurations, Including the Tidal Boundary Conditions, the Geometric Latitudes (i.e., Testing the Coriolis Force), the Manning Coefficients, and the Initial Bed Slopes (the Blanks Indicate the Same Parameter as Run REF)*

| | Tidal boundary | | | | | | | | | |
|---|---|---|---|---|---|---|---|---|---|---|
| Run ID | M2 tide | P1 | P2 | P3 | P4 | P5 | P6 | Latitude (°N) | Manning coefficient ($s/m^{1/3}$) | Initial bed slope (‰) |
| REF | AMP (m) | 1.0 | 1.05 | 0.75 | 0.60 | 0.45 | 1.05 | Real | 0.015 | 0.180 |
| | Phase (°) | 0 | 12 | 45 | 90 | 180 | 270 | | | |
| T1 | AMP (m) | 1.0 | 1.05 | 0.75 | 0.60 | 0.45 | 1.05 | | | |
| | Phase (°) | 0 | 54 | 108 | 162 | 216 | 270 | | | |
| T2 | AMP (m) | 0.75 | 0.75 | 0.75 | 0.75 | 0.75 | 0.75 | | | |
| | Phase (°) | 0 | 12 | 45 | 90 | 180 | 270 | | | |
| T3 | AMP (m) | 0.75 | 0.75 | 0.75 | 0.75 | 0.75 | 0.75 | | | |
| | Phase (°) | 0 | 0 | 0 | 0 | 0 | 0 | | | |
| C1 | | | | | | | | 20 | | |
| C2 | | | | | | | | 10 | | |
| C3 | | | | | | | | 0 | | |
| R1 | | | | | | | | | 0.010 | |
| R2 | | | | | | | | | 0.020 | |
| R3 | | | | | | | | | 0.025 | |
| S1 | | | | | | | | | | 0.167 |
| S2 | | | | | | | | | | 0.153 |
| S3 | | | | | | | | | | 0.130 |

*Note*. "AMP" denotes amplitude; REF is the reference run, of which the simulated configurations at the end look most like the real radial sand ridges. The "real latitude" means that the latitude varies spatially depending on the position of the cells in the model (from 30.7°N to 35.2°N). The "initial bed slope" represents the second part of the profile as shown in Figure 1d.

deep-water one gently reducing the slope to zero (Figure 1d). These characteristically represent the overall variation of the bed elevation from the land to the sea (Figure 1b). Notice that the present-day RSRs have portions above the mean sea level that are exposed during low tide but that those are not represented in the initial model bathymetry. The grain size $D_{50}$ is set as 125 μm, according to the observation data (Zhang, 2012). In fact, the changing $D_{50}$ has the same effects as changing the geomorphic factor in the numerical model, since Engelund and Hansen (1967) formula is used (as pointed out by, e.g., Dissanayake et al., 2009; Van der Wegen et al., 2008; Zhou, Olabarrieta, et al., 2014). Other physical parameters, such as the Manning coefficient (=0.015 $s/m^{1/3}$), and the horizontal eddy viscosity coefficient (=1 $m^2/s$), are set following previous studies (e.g., Xing et al., 2012; Xu et al., 2016). At the seaward boundary, an "equilibrium boundary condition" technique is employed that the sediment load passing through the boundaries is "perfectly" adapted to the local flow. As a result of considerably large water depths, the erosion or deposition along the seaward boundary is negligible (e.g., Van der Wegen et al., 2008). This technique does not imply that the total amount of sediments is conserved within the computational domain, because sediment fluxes are allowed to pass through the boundary.

Four sets of additional runs are presented to analyze the effects of the tidal boundary condition (T1–T3), the Coriolis force (C1–C3), the Manning coefficient (i.e., the bed resistance, R1–R3), and the initial water depths (S1–S3) on the morphodynamics of the RSRs. All the runs are listed in Table 1 varying one model parameterization based on the reference case (run REF). For runs S1–S3, smaller initial water depths imply larger sediment supply, since the water depths are determined by the accumulation of sediments. In this way, run S3 is of more sediment distributed in the outer sea and less in the central region. Moreover, smaller initial water depths also lead to higher sediment transportability, because the tidal flow is constrained in shallower water, which results in larger current velocities. Sorting by the average water depth from high to low, we get S2 > S1 > S3 = REF. Notice that varying the initial water depths in runs S1 and S2 is accompanied by changes of bed slopes, which interfere with the analysis on the initial water depths. Therefore, run S3 is designed with a smaller initial bed slope and the same averaged initial water depths compared with run REF. This implies that run S3 initially is of more sediment distributed in the outer sea and less in the central area than run REF. All the runs are simulated for 2,000 years with the time step of 2 min. Notice that the time scale "2,000 years" here is just conceptual for the system to approach a dynamic equilibrium (as argued by Zhou et al., 2017). Considering the gap between hydrodynamic and morphodynamic processes time scales,

the morphodynamic evolution is scaled up linearly by a geomorphic factor (=200; Roelvink, 2006). Typical values of this factor for sandy environments may range from tens to hundreds (e.g., Dastgheib et al., 2008; Ranasinghe et al., 2011; Van der Wegen & Roelvink, 2008).

## 4. Results

### 4.1. The Simulated Morphodynamic Evolution

The simulated geomorphic patterns of run REF at years 100, 500, 1,000, and 2,000 are shown in Figure 3 (see the Supporting Information for a dynamic view). At year 100, a series of thin sand ridges are formed near the landward apex, where the tidal current velocities are relatively large due to the convergence of the tidal system waves. The sand ridges are elongated in the north and relatively short in the south. This spatial variation in the length of the sand ridges is related to tidal flow pattern: bidirectional in the north and rotational in the south (Figure 2b). Sediments continuously accrete in the central region of the RSRs and the sand ridges near the apex gradually merge, leading to the formation of several huge sand bodies (Figures 3b and 3c). After 2,000 years, the spatial patterns of the sand ridges tend to be stabilized and show similarly radiated planar forms as the real RSRs in terms of the length scales and the spatial curvatures (Figures 3d and 3e).

To clarify whether the present system converges to a morphodynamic equilibrium (Zhou et al., 2017), we quantify the morphodynamic evolution using the mean square root of the overall variations in bed level relative to the initial state (as, e.g., Garnier et al., 2006; Nnafie et al., 2014):

$$\Delta z_{\mathrm{rms}}(t) = \sqrt{\frac{1}{A}\iint_A [z_t(x,y,t) - z_0(x,y)]^2 \mathrm{d}x\mathrm{d}y}, \tag{2}$$

where $A$ is the total planar area of the embayment, and $z_0(x,y)$ and $z_t(x,y,t)$ are the bed surface elevations at time 0 and $t$, respectively. The morphodynamic evolution can also be considered as a self-organized process tending to minimize the energy dissipation caused by, for example, the bed resistance and sediment transport (Rodríguez-Iturbe et al., 1992). The mean energy dissipation is calculated following the expression proposed by Van der Wegen et al. (2008):

$$E_d = \frac{1}{A}\iint_A \left[\left|\rho_{\mathrm{w}} g n^2 U^3 \sqrt[3]{\frac{1}{H}}\right| + \left|\frac{0.05}{\Delta D_{50}}\rho_{\mathrm{w}}\sqrt{g} n^3 \frac{U^5}{\sqrt{H}}\right|\right] \mathrm{d}x\mathrm{d}y \tag{3}$$

The time series of the quantified bed evolution $\Delta z_{\mathrm{rms}}$ and the total energy dissipation $E_d$ over the 2,000-year simulation period are shown in Figure 4. The energy dissipation is relatively high at the beginning of the simulation, which implies that the initial bed morphology is far away from the equilibrium configuration (Van der Wegen & Roelvink, 2008; Zhou, Coco, et al., 2014; Zhou, Olabarrieta, et al., 2014). Correspondingly, the system experiences pronounced evolution with $\Delta z_{\mathrm{rms}}$ increasing and $E_d$ decreasing rapidly in the first 200 years. As the radial channel-ridge patterns are formed between years 100 and 500 (Figures 3a and 3b), the variations of $\Delta z_{\mathrm{rms}}$ and $E_d$ are both reduced, indicating that the interaction between the tidal flow and the bed topography progressively becomes milder. Around the year 1,500, the variation of $\Delta z_{\mathrm{rms}}$ is minimal, and the energy dissipation $E_d$ maintains at a low level. Therefore, it can be inferred that the system asymptotically converges to morphodynamic equilibrium.

### 4.2. The Equilibrium Configuration

Figure 5a shows the cotidal chart of the $M_2$ constituent in run REF calculated using the initial bathymetry. The model successfully reproduces the typical tidal wave systems, which are characterized by an amphidromic point located in the north and the convergence of the tidal system waves to the central area (e.g., Zhang et al., 1999). The tidal ellipses show a fan-shaped pattern with their major axes mainly oriented toward the center of the embayment. Moreover, the bidirectional and rotational tidal currents, respectively, occupy the north and south of the embayment (Figure 5b), which is also consistent with the tidal current fields over the RSRs (Figure 2b). Some small differences are observed between the modeled and real RSRs. For example, modeled southern tidal currents are somewhat less elliptical than those in the real RSRs. This can be attributed to the land boundary, which extends farther seaward than the real coast (see Figure 1b) and restricts the component of the tidal flow in its normal direction. The resultant year 2,000 sand ridges show a similarly

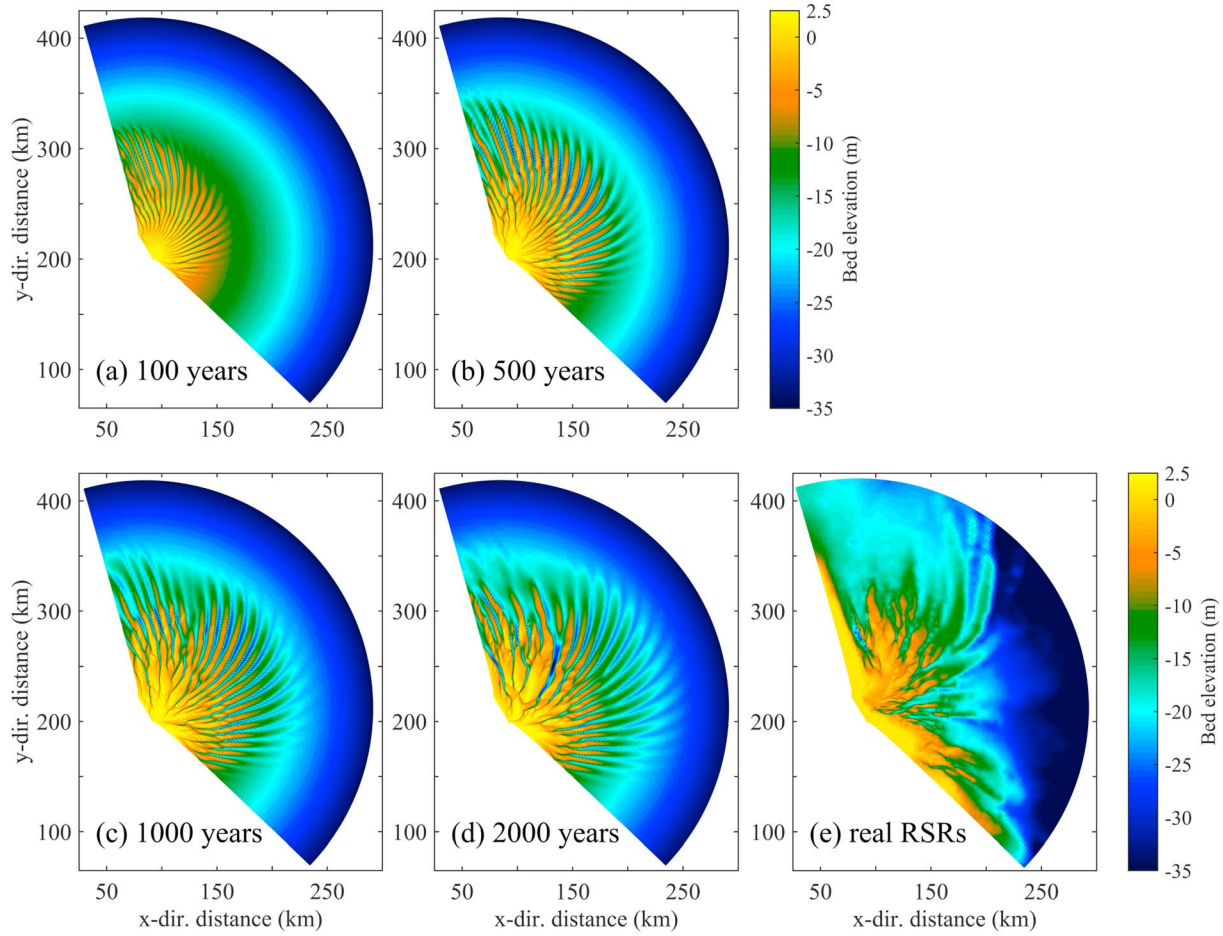


**Figure 3.** Morphologies simulated in (a–d) run REF and of (e) the real RSRs. RSRs = radial sand ridges.

radiated spatial pattern and planimetric scale as the real RSRs (comparing Figure 3d with Figure 3e). The sand ridges located in the north are elongated, while those in the south are relatively short, which correspond to the distribution of the tidal ellipses (Figures 5b and 5e). The sand ridges are bending

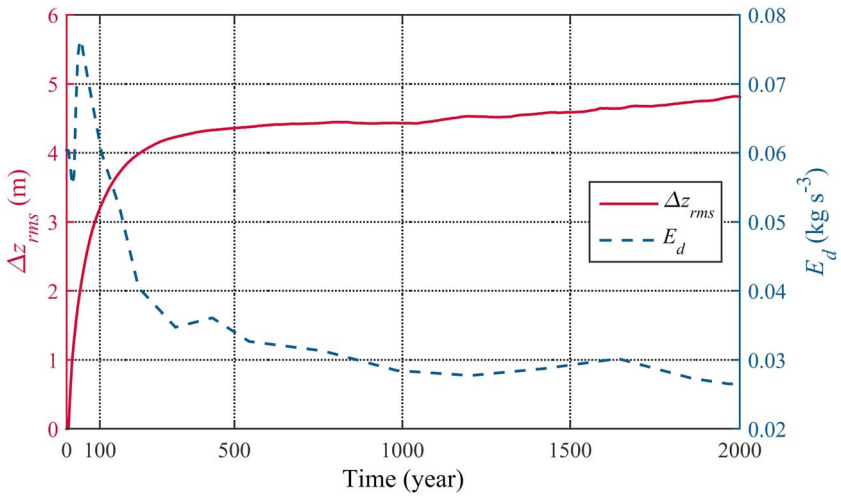


**Figure 4.** Time series of the overall variation of the $z_{rms}$ and the energy dissipation per unit area $E_d$ averaged over a tidal cycle.

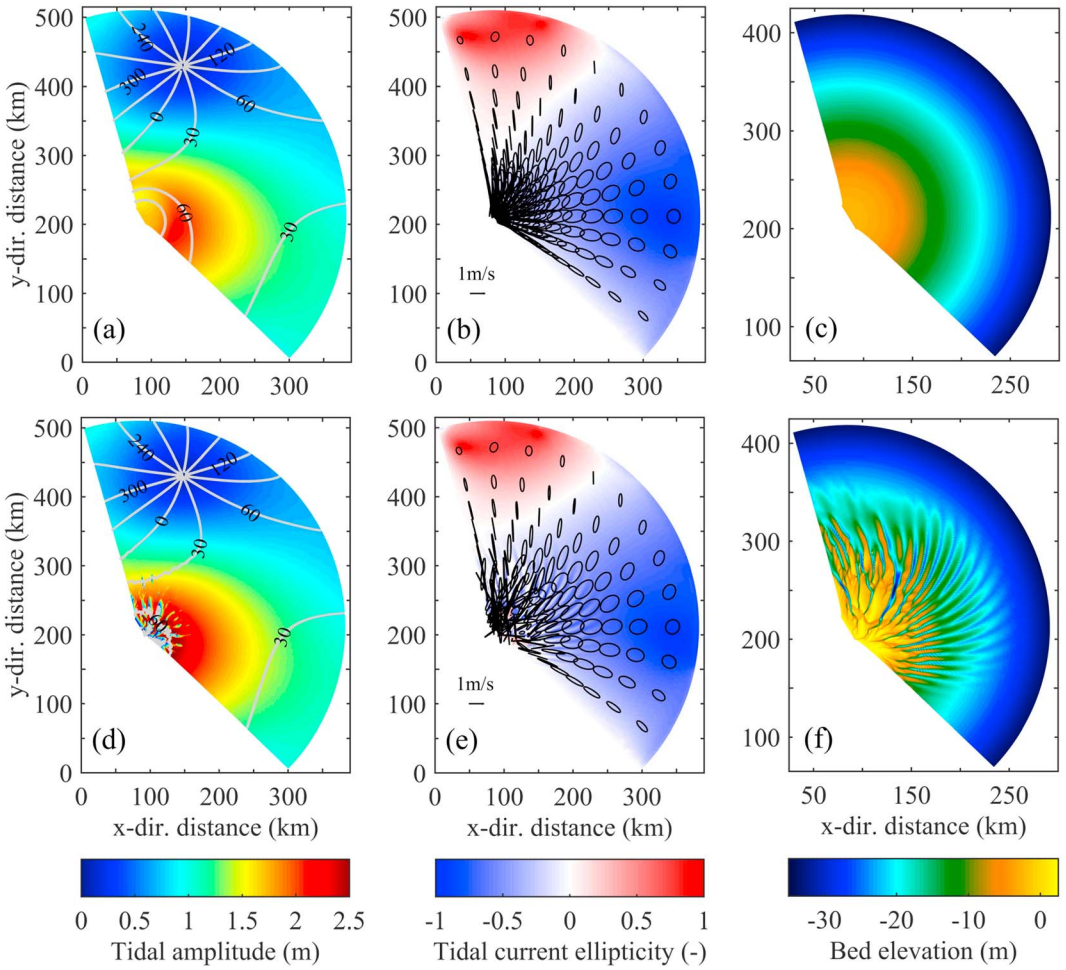


**Figure 5.** (a) Cotidal charts and (b) the tidal current ellipses of the $M_2$ tidal constituent and (c) the morphology at year 0 simulated in run REF. (d)–(f) show their year 2,000 counterparts. The year 2,000 phase lines are relatively intricate at the apex due to the complicated bed topography.

anticlockwise, which is related to the rotations of the tidal ellipses in the centrifugal direction (Figure 5b). The differences in the tidal regimes between years 2,000 and 0 mainly concentrated in the central area, which is attributed to the complicated bed topography (Figure 5d). However, the overall patterns of phase lines and tidal ellipses are not significant affected by the geomorphic change (cf. Figures 5a and 5b with Figures 5d and 5e). Therefore, the analysis hereafter is based on the tidal regimes at year 0.

Huthnance (1982a) suggested an approximately 28° angle between the orientations of bidirectional tidal currents and sand ridge crests for tidal sand ridges. However, the tidal currents are not strictly bidirectional over the RSRs. Instead, the tidal regime and the sand ridges show complicated patterns and remarkable regional differences between the south and the north (Figure 5). In order to clarify the relationships between the tidal currents and the sand ridges in their orientations, a series of elongated sand ridges with clear crest lines spreading outside the huge sand bodies are analyzed for run REF (Figure 6a). A least squares method is applied to fit the best ellipses to the tidal vector trajectories, and their long axes are used as the main directions of the tidal currents (Figures 6b and 6c). The local orientations between the tidal current (denoted as "$\theta_f$") and the sand ridge crest (denoted as "$\theta_c$") are compared in Figure 6d (10 points are sampled on each crest). The sampling points mainly fall into two groups characterized by $\theta_f \approx \theta_c - 28°$ (black circles) and $\theta_f \approx \theta_c$ (red triangles). The spatial distributions of these two types of sampling points are shown in Figure 6a. Both relationships are also observed in numerical studies which focus on the tidal current in the RSRs (e.g., Xu et al., 2016). The sand ridge crests following $\theta_f \approx \theta_c - 28°$ mainly locate in the north and the south ends of the embayment (see the black circles in Figure 6a), where bidirectional tidal

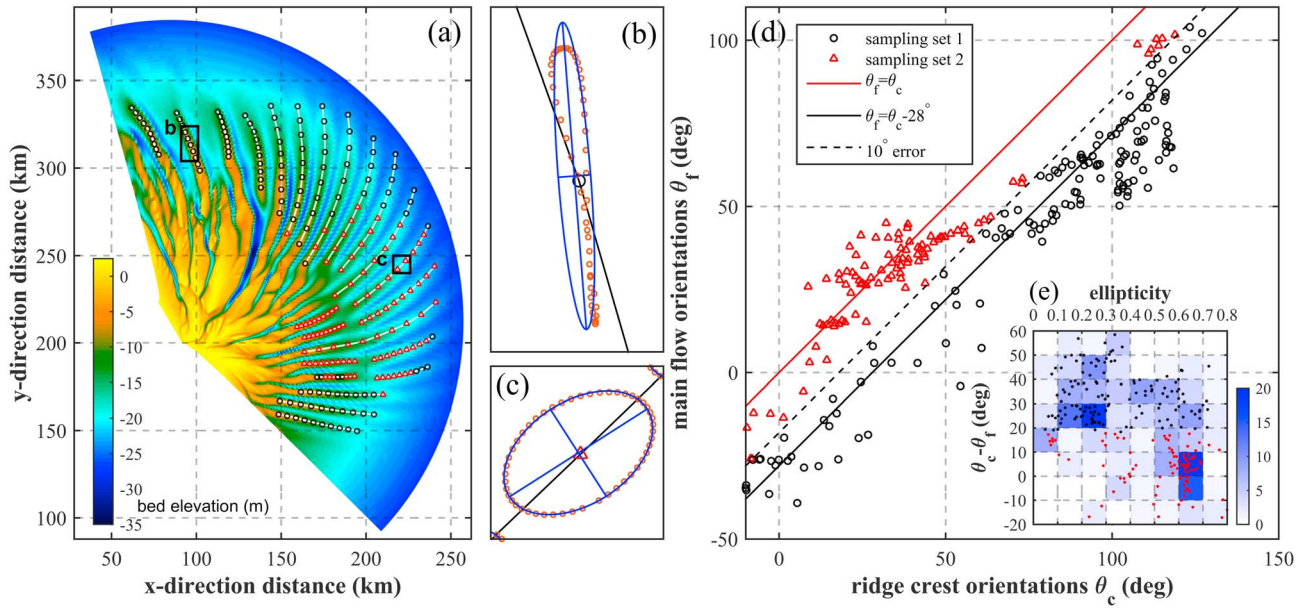


**Figure 6.** Comparison between orientations of the sand ridges and the main directions of the tidal currents simulated in run REF. (a) indicates the locations of the sampled sand ridge crests, on each 10 points are sampled. (b) and (c) illustrate the determination of the main directions of the tidal currents through the best fitting oval (the blue ellipses) to the tidal vector trajectories (the red circles). The black lines indicate the sand ridge crests. The main directions of the tidal currents are approximated by the long axes of the ovals. (d) compares the orientations of the sand ridges $\theta_c$ and the main directions of the tidal currents $\theta_f$. The sampling points showing $\theta_f \approx \theta_c - 28°$ (as suggested by Huthnance, 1982a) are marked in black. The rest ones are marked in red, which indicate $\theta_f \approx \theta_c$. These two sets of sampling points are separated by the black dashed line, which indicates a 10° offset from $\theta_f = \theta_c - 28°$. (e) shows the distribution of all sampling points in an angle-ellipticity plane. The color code shows the number of points within the range (i.e., density).

currents prevail. The other ones indicating $\theta_f \approx \theta_c$ are situated in the midsouth part (see the red triangles in Figure 6a), which are dominated by rotational tidal currents. Figure 6e shows the distribution of the sampling points in an angle-ellipticity plane, in which the color code indicates the number of points within an elementary area (i.e., density). The angle $\theta_c - \theta_f$ overall shows a decrease tendency with the increase of the ellipticity. Moreover, the sampling points concentrate in two regions: (1) $20 < \theta_c - \theta_f < 30$ and $0 < E < 0.3$ ($E$ denotes the ellipticity), which indicates bidirectional tidal currents; and (2) $-10 < \theta_c - \theta_f < 10$ and $0.6 < E < 0.7$, which represents rotational tidal currents. Notice that the orientations of the sand ridge crests are in fact difficult to be exactly identified, since the morphology is complicated and the top of the sand ridges is flat. This may result in the relatively scattered distribution of sampling points in Figures 6d and 6e.

To further evaluate the performance of the numerical model, the number of sand ridges simulated in run REF are compared with the real RSRs. The sand ridges are counted along 15 radial sections centered on the apex with radiuses increasing from 10 to 150 km (Figure 7). The total number of the sand ridges is overestimated by the numerical model, especially in the seaward sections (radius larger than 110 km), where the total number does not decrease as significantly as the real RSRs. It can be hypothesized that the implicit sediment supply is excessive in the model and that sand ridges can extend longer than the real ones. However, the overall variation tendency is consistent with the real RSRs such that the total number initially increases and then decreases, peaking at approximately 70 km (Figure 7e).

### 4.3. Analysis of Parameter Space Variables

In addition to the reference simulation examining the correspondence between the tidal regime and the radial morphology of the RSRs, four sets of numerical experiments are performed to analyze the effects of the tidal boundary conditions (runs T1–T3), the Coriolis force (runs C1–C3), the bed resistance (runs R1–R3), and the initial water depths (runs S1–S3) on the tidal regime and the morphology of the RSRs. Since the overall tidal regimes are not affected significantly by bed topography (Figure 5), the tidal ellipses and tidal phase lines at year 0 are considered for ease of analysis.

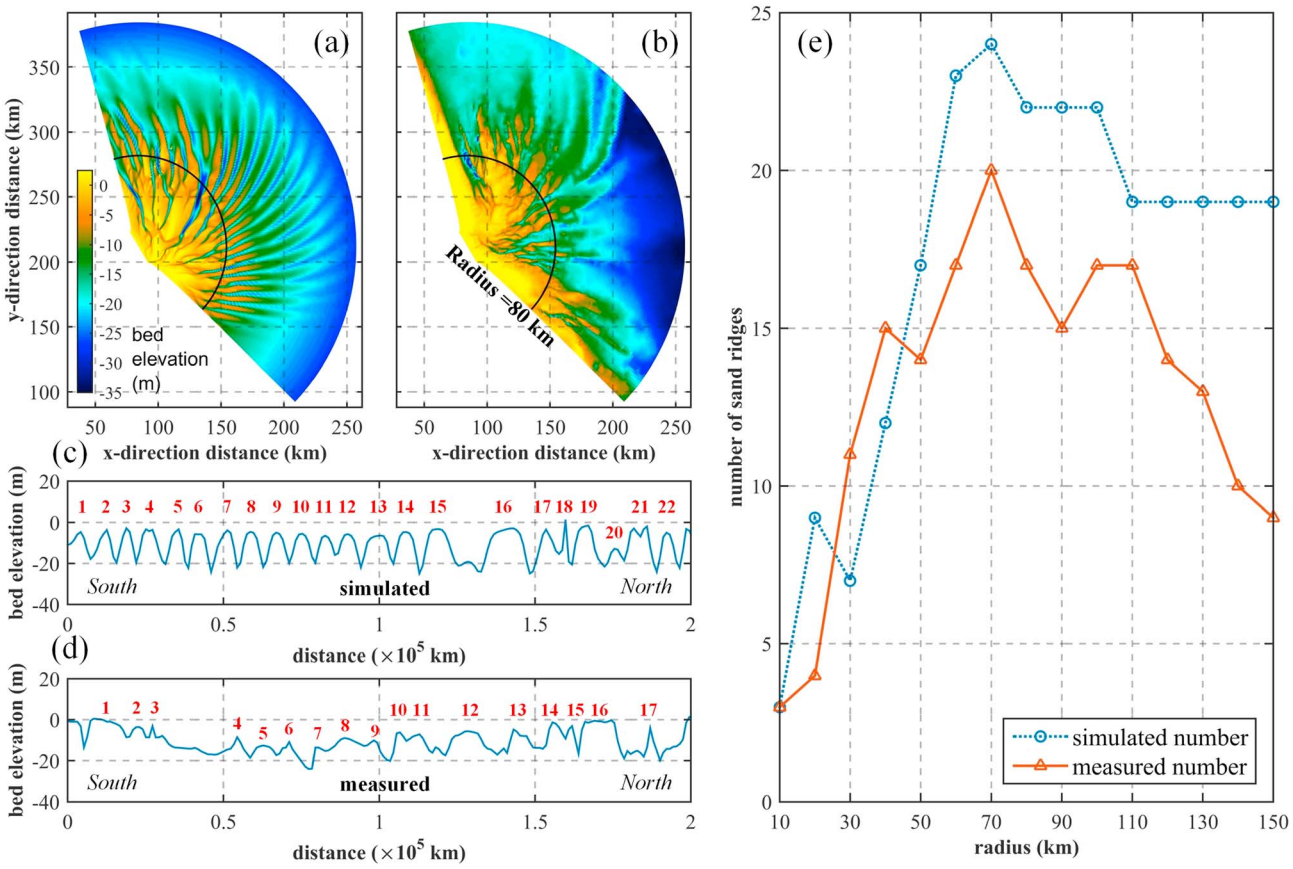


**Figure 7.** Comparison in the sand ridge numbers between run REF and the real radial sand ridges. (a) The year 2,000 bathymetry simulated in run REF. (b) The measured bathymetry of the radial sand ridges. (c, d) The bed elevations and the correspondent sand ridge numbers at the cross section with the radius of 80 km (see the black arc line in (a) and (b)). (e) The sand ridge numbers at 15 cross sections with the radius varying from 10 to 150 km.

The tidal phase is modified linearly varying from 0° to 270° along the seaward boundary in run T1. The amphidromic point moves close to the central area, so that the tidal amplitude is reduced (Figure 8b). Correspondingly, the sand ridges are not well developed, and the overall size of the geomorphic pattern is reduced (Figure 8f). In run T2 with constant amplitude along the seaward boundary and the same phase lag as run REF, similar phenomena are observed: The tidal wave is less concentrated, and the overall sand ridges are not well developed (Figures 8c and 8g). The tidal wave directly converges to the center of the embayment in run T3, since both the tidal amplitude and phase are uniform along the boundary (Figure 8d). This leads to the largest tidal amplitudes and the most pronouncedly developed sand ridges among all the scenarios (Figures 8d and 8h). However, these sand ridges are overall radially distributed, while the asymmetric pattern in reality is not reproduced (Figure 8h).

The amphidromic point shifts landward as the latitude decreases (i.e., the Coriolis force decreases; Figure 8 i). When the latitude is set 10°N or smaller (i.e., runs C2 and C3; Figures 8j and 8k), the amphidromic point vanishes, such that the tidal wave almost directly propagates across the embayment from south to north rather than converging to the central area. Without the constraint of the amphidromic point, runs C2 and C3 are of larger tidal amplitude in the central area than run REF. Therefore, huge sand bodies instead of elongated sand ridges are formed in the north of the embayment (Figures 8m and 8n). Since the main directions of tidal currents do not orient to the center of the embayment, the sand bodies do not show radial pattern (Figure 8n).

An increase in bottom friction leads to decreases in the magnitudes of tidal amplitudes and tidal current velocities and, hence, a decrease in the sediment transport by tidal flow. Correspondingly, runs R2 and R3, which adopt relatively large friction coefficients, indicate smaller sizes of tidal sand ridges than those of run REF (Figures 9g and 9h). Moreover, varying the friction coefficient changes the location of the

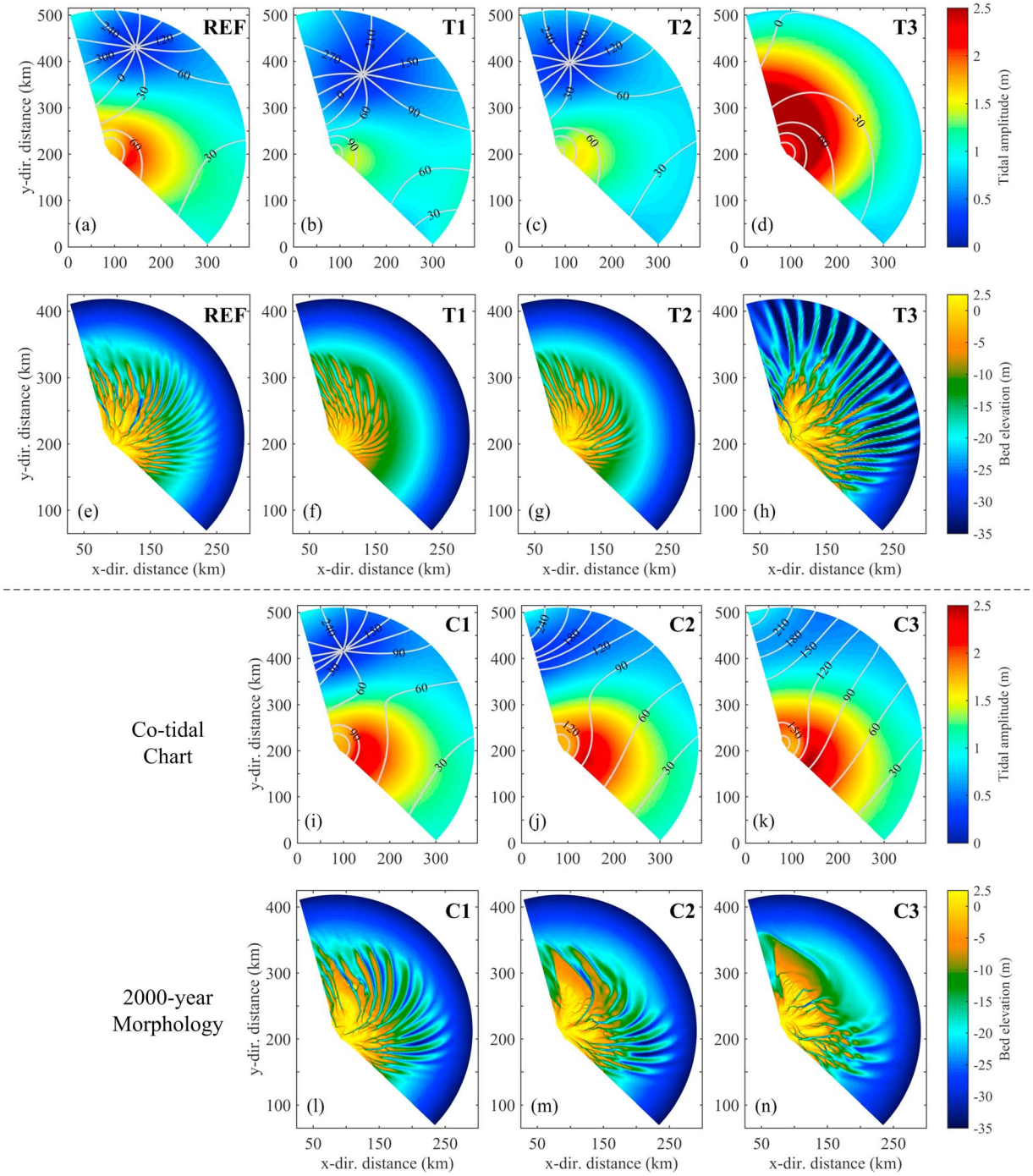


**Figure 8.** Comparison between run REF and runs T1–T3 and C1–C3 on the cotidal charts of the M2 tidal constituent (a-d and i-k) and the resultant morphologies at year 2,000 (e-h and l-n). The reader is referred to Table 1 for detailed model setup.

amphidromic point (Figures 9a–9d), such that the overall tidal wave system and its associated tidal current fields are affected. This further leads to several different characteristics of the sand ridges from run REF, such as the orientation and the bending (Figures 9e–9h). Notice that the Manning coefficient used in run R3 (0.025 $s/m^{1/3}$) is a common value adopted in coastal areas (e.g., Soulsby, 1997). However, much less and smaller sand ridges are reproduced. This leads to a hypothesis that the reduction of the hydraulic drag due to high sediment concentration is relevant for the formation of the RSRs (e.g., the drag reduction suggested by, e.g., Winterwerp & Wang, 2013; Winterwerp et al., 2013).

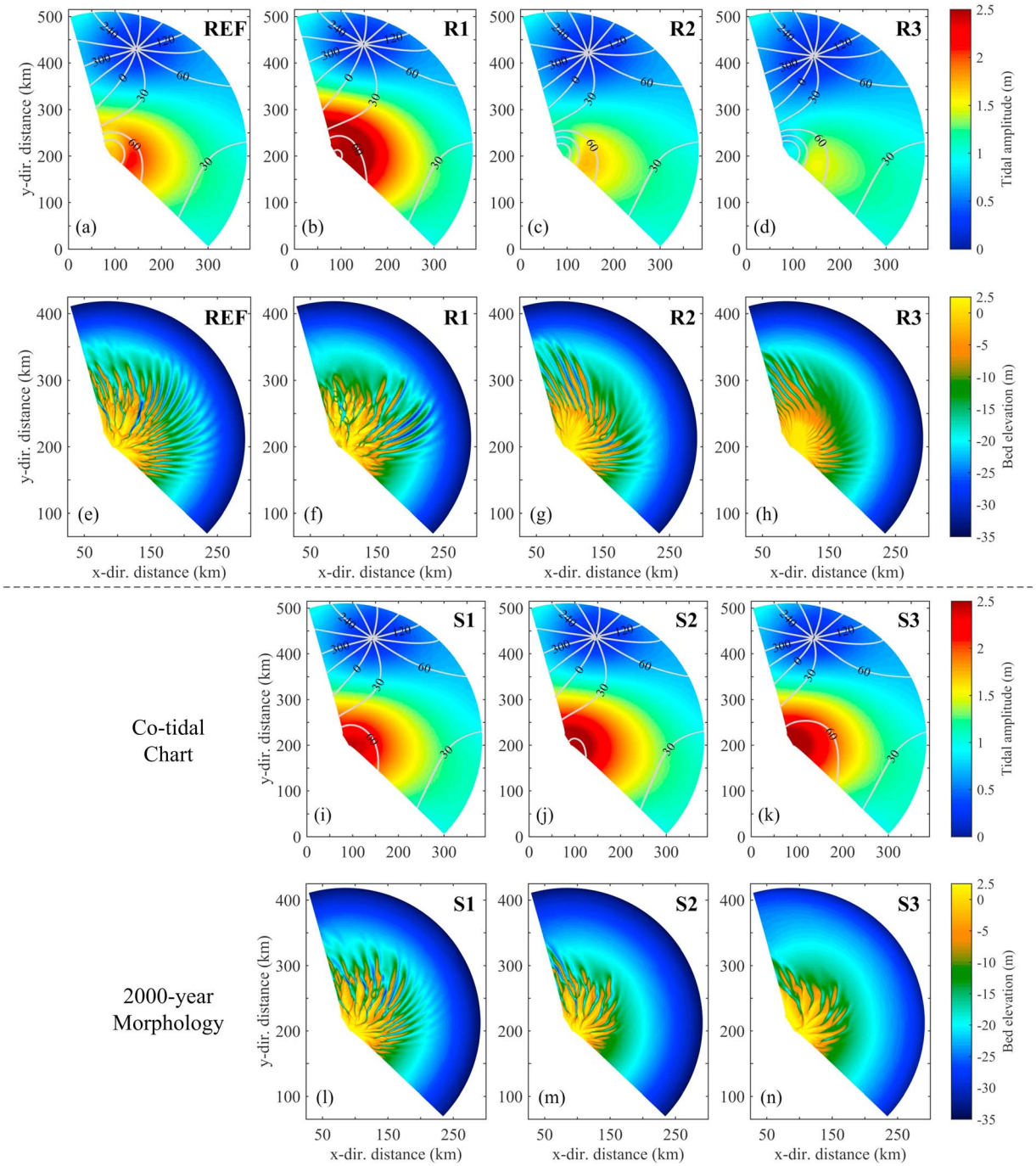


**Figure 9.** Comparison between run REF and runs R1–R3 and S1–S3 on the cotidal charts of the M2 tidal constituent (a-d and i-k) and the resultant morphologies at year 2000 (e-h and l-n). The reader is referred to Table 1 for detailed model setup.

Runs S1 and S2 indicate that both the sizes and the number of the simulated sand ridges decrease as the initial water depth increases (Figures 9l and 9m). This is consistent with the suggestion proposed by Off (1963) that the development of sand ridges favors abundant sediment supply. Run S3 (Figure 9n) also shows smaller and less sand ridges than run REF, even though their averaged initial water depths are the same. Notice that the only difference between these two runs is that the initial bed slope of run S3 is smaller than run REF.

## 5. Discussion

### 5.1. Tidal Regime, Sediment Supply, and Morphology

It has been suggested that the formation of the rotational tidal-system wave in the north of the RSRs results from the constraint by the eastern coastline of China, such as the reflection of the tidal waves by Shandong Peninsula (Zhang et al., 1999). The constraint by the coastlines is not explicitly considered but implicitly represented by the tidal boundary conditions in the present model (Figure 1b). As shown in runs T1 and T2, modifying the phases or the amplitudes along the seaward boundary shifts the position of the amphidromic point and further results in limited development of sand ridges. Moreover, the magnitude of the Coriolis force, which is determined by the geographic latitude, also considerably affects the tidal wave systems and the formation of linear sand ridges (runs C1–C3; see Figure 8). Therefore, both the current tidal regime and the morphology of the RSRs depend on the east coastline of China as well as their specific geographic latitude.

The effects of sediment supply and current velocities, which have been suggested crucial in forming tidal sand ridges (e.g., Off, 1963), are implied in runs S1–S3 and R1–R3, respectively. The sediment transport capability of the tidal current is low in the runs with relatively large Manning coefficient (i.e., runs R2 and R3). Therefore, the resultant morphology indicates that both the development of sand ridges and the accretion of sediment in the central area are limited (Figures 9g and 9h). When simulating with large initial water depths (i.e., runs S1 and S2), large sand bodies are formed in the central area (Figures 9m and 9n), which is attributed to the convergence of the sediments driven by the tidal regime. However, the seaward extension of the sand ridges is limited. The comparison between runs S3 and REF further suggests that the sediment from outer sea is less efficient than those near the coast in forming of the RSRs. This result highlights the contribution of the littoral sediment transport to the development of the RSRs, such as the sediment supply from the Abandoned Yellow River Delta (as suggested by Du et al., 2018; Wang, Zhang, et al., 2012).

### 5.2. The Asymmetric Pattern of the RSRs

One of the typical characteristics of the RSRs is their asymmetric pattern showing larger northern sand ridges than the southern ones (Xu et al., 2016). Therefore, we are motivated to divide the computational domain into two halves from the middle radial line (see the black bold line in Figure 10a) and compare the planar areas of the sand ridges between the northern and southern parts (Figures 10b and 10c). We calculate the areas of the regions with water depth smaller than 5 and 10 m respectively, for the consideration of the underwater sand ridges (see black and red contour lines in Figure 10a). The 10-m areas of run REF indicate a favorable distribution consistent with the real RSRs. Moreover, both the 5- and 10-m areas of run REF agree well with the real RSRs in magnitude. On the other hand, most runs with parameters modified exhibit less consistency with the real RSRs, which highlights the rationality of the parameterizations selected in the run REF.

The major sediment source for the present-day RSRs came from the Abandoned Yellow River Delta in the north (Du et al., 2018; Wang, Zhang, et al., 2012). However, run REF starts from equally distributed water depths (i.e., sediment supply) between the south and the north. As a result, the 5-m area of run REF appears to be smaller in the north than that in the south, which is inconsistent with the real RSRs. It thus can be inferred that the larger size of the northern sand ridges over the southern ones is partly attributed to the unequal sediment supply between the south and north. On the other hand, the consistency indicated by the distribution of the 10-m area of run REF confirms that the tidal regime over the RSRs does prefer a larger scale of the northern sand ridges than the southern ones.

When the rotational tidal wave vanishes and hence the entire embayment is dominated by the progressive tidal wave (run C3; Figure 8k), the advantage in size of the northern area over the southern one is amplified (Figures 8n, 10b, and 10c). It can thus be inferred that the asymmetric pattern of the RSRs is promoted by the progressive tidal wave system in the south while is restricted by the rotational one in the north. However, run C3 does not show elongated sand ridges as presented in the real RSRs. This implies that the RSRs cannot be formed without the convergence of the tidal wave system to the central region.

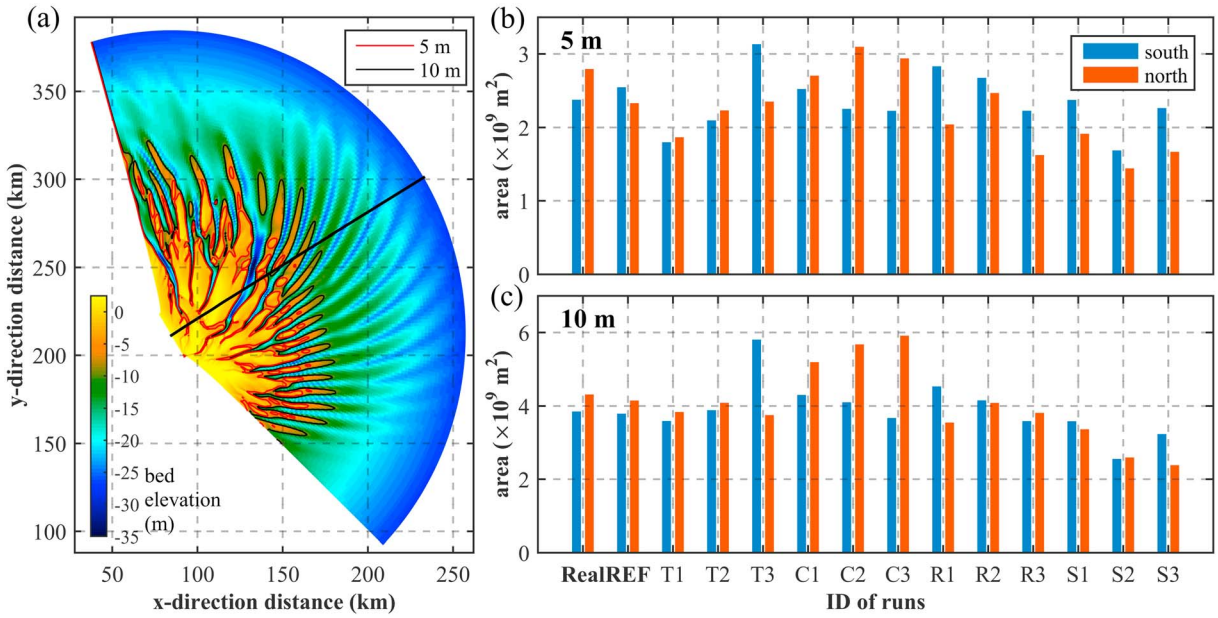


**Figure 10.** Comparison of the sand ridge areas between the real radial sand ridges and the numerical runs. (a) illustrates the method of calculating the areas of the southern and the northern sand ridges. The computational domain is divided into southern and northern halves from the middle radial line (see the black bold line). (b) and (c) illustrate the planar areas enclosed by the 5- and 10-m contour lines, respectively.

### 5.3. Comparison With Other Sand Ridges

Sand ridges over the world have a wide variety of forms due to the difference in hydrodynamic and sediment regimes (Dyer & Huntley, 1999; Off, 1963). However, the growth of sand ridges always requires mechanisms that drive the sediment flux to converge to the ridge crest and to diverge from the channels (e.g., Calvete et al., 2001; Huthnance, 1982a, 1982b). In this section, the mechanisms underlying the formation of the RSRs are compared with two typical categories of sand ridges, namely, the linear sand ridges (e.g., Hulscher et al., 1993) and the shoreface-connected sand ridges (e.g., Swift, 1975).

The linear sand ridges (also known as "linear sand banks") generally occur in open shelf seas, where oscillatory tidal currents prevail. The offshore sand ridges lying on the seabed of the North Sea are representative linear sand ridges, of which the dimensions are typically tens of kilometers long, several kilometers broad, and tens of meters high, and the directions slightly deviate from the principle axis of the tidal ellipses. It has been shown that linear sand ridges can be formed on a flat seabed under back-and-forth tidal movements and a faster-than-linear sediment transport rate related to the tidal current velocity (Hulscher et al., 1993; Huthnance, 1982a, 1982b). A possible mechanism leading to the positive feedback between the tidal currents and the erodible seabed has been given (Huthnance, 1982a): When the tidal current moves over a sand ridge, which cyclonically rotates with respect to the main current direction, an anticyclonic residual circulation can be formed around the sand ridge by both the Coriolis and frictional torques. Both torques vanish at the ridge crest, such that sediment can be accreted exactly on the ridge crest.

The shoreface-connect ridges are usually observed on storm-dominant inner shelves, where net longshore currents are strong. There are significant geomorphic differences between the storm-induced ridges (i.e., shoreface-connected ridges) and tide-induced ridges (i.e., tidal sand ridges). The spatial sizes of tide-induced ridges are evidently larger than those of the storm-induced ridges. On the other hand, the orientations of the tidal sand ridges are cyclonically rotated with respect to the major directions of the tidal currents, while the orientations of the shoreface-connected ridges are primarily related to the orientations of the coastlines. The formation of the shoreface-connected ridges has been attributed to the presence of the residual longshore currents and the transversal seabed slope in the inner shelf regions. Since the seabed is inclined, the Coriolis and frictional torques do not vanish as in the flat bed case. Therefore, the anticyclonic residual circulation is constrained to the coastlines (Calvete et al., 2001; Trowbridge, 1995).

The RSRs have been classified as tide-induced sand ridges formed during Holocene transgression (Wang et al., 1999; Yang, 1989). The stationary tidal wave system covering the South Yellow Sea, which has been suggested to be crucial for the formation of the RSRs, has been demonstrated to exist since the early Holocene (Wang, Zhang, et al., 2012; Zhang et al., 1999). Although the ends of the RSRs connect to the Jiangsu Coast, which seems to be similar with the shoreface-connected ridges, the hydrodynamic regime and the spatial dimensions of the RSRs apparently differ from those of the shoreface-connected ridges (Wang, Zhang, et al., 2012). Comparatively, acting as tidal sand ridges, the RSRs represent evidently tidal-sand-ridge characteristics. For example, the orientations of the sand ridges are anticlockwise deviating from the major directions of the tidal currents (Figure 6; Huthnance, 1982b), and the sizes of the seaward parts of the sand ridges are in accordance with tidal sand ridges (Wang et al., 1999).

On the other hand, the RSRs, which are situated at a semiopen sea area, differ from those tidal sand ridges observed in open sea regions (e.g., the North Sea) remarkably in terms of their fan-shaped spatial patterns and the huge exposed sand bodies in the central region (Figure 1b, see also Wang, Zhang, et al., 2012). Controlled by both the land boundaries of China and Korea Peninsula and the slope of the South Yellow Sea Shelf, the tidal waves converge to the central region of the RSRs and further produce the distinct fan-shaped tidal current field covering this region (Qian et al., 2015). Correspondingly, as shown in Figure 3a, the sand ridges, which are formed in the early stage of the simulation, are radially distributed with their spacing diminishing landward, rather than approximately parallel to each other (as, e.g., North Sea). As the sediments continuously accumulate in the central region owing to the landward residual movements of the sediment (Xing et al., 2012), the channels between the sand ridges are filled up, and hence, the landward parts of the sand ridges merge and finally expose above the water surface (Figures 3b–3d). Overall, the RSRs are tide-induced sand ridges, while the geomorphic details are determined by their specific geographical position and the typically fan-shaped and converging tidal current fields.

### 5.4. Model Capability and Further Research

The idealized model used in this study is developed based on the current tidal regime over the RSRs. A 2-D framework is used considering the temporal and spatial scale concerned. This can help us to understand the relationship between the present tidal regime and morphology of the RSRs. However, this model does not aim to solve the controversy related to the origin of the RSRs (Li et al., 2001; Wang et al., 1999; Wang, Zhang, et al., 2012), because the historical transitions of the coastline (e.g., the Jiangsu coastline) and the sediment source (e.g., the migration of the Yellow River mouth; Wang, Zhang, et al., 2012) remain elusive. Moreover, the current boundary condition implies limited external sediment supply. Therefore, the model cannot be used to explain whether the sediments are from the Yangtze River (Milliman et al., 1986; Wang, Zhang, et al., 2012) or the Yellow River (Lee & Chough, 1989; Saito & Yang, 1994; Zhou, Liu, et al., 2014). In addition to the simplifications related to the idealized modeling configurations, several processes that may play a certain role in shaping the RSRs are neglected and deserve further research.

1. Only noncohesive sand with a single representative grain size of 125 μm is considered in the model, while the RSRs are characterized by the presence of mixed grain sizes from very fine sand to fine sand (Zhang, 2012). The modeled sand ridges are more irregular than the simulated ones, because of the homogeneous bed sediment configurations used in the present model. On the other hand, processes such as sediment sorting and sand-mud interactions should be addressed in future research, which can play an important role on the morphodynamic evolution of sand ridges (De Swart et al., 2008; Vis-Star et al., 2009).
2. Winds and wind-driven waves are not considered. Previous studies have shown that wind-driven waves affect the morphology of sand ridges (Calvete et al., 2002), particularly during low tidal levels (Reynaud et al., 1999). Similarly, storm surges have been found to effectively modify the morphologies of the sand ridges in the short term (Calvete et al., 2001), while tidal currents act as a restoring force in the long term (Zhang et al., 1999).
3. The effect of long-term sea-level rise and riverine sediment supply is not considered in this model, although it has been argued that they played an important role in the evolution of tidal sand ridges (Gao, 2013; Uehara et al., 2002; Uehara & Saito, 2003; Wang, Zhang, et al., 2012). Sensitivity simulations of Nnafie et al. (2014) indicate that a rising sea-level results in an increasing height of sand ridges. At the same time, their simulated results suggest that sand ridges do not form if the rate of the sea-level rise is too high or if the initial depth of the inner shelf is too small. On the other hand, major rivers can affect the

long-term morphodynamic evolution of the RSRs by favoring sediment deposition and modifying the local morphology near the outlet (Zhou, Coco, et al., 2014), which should be properly considered in further research.

4. Extensive human interferences (e.g., the large-scale land reclamations along the Jiangsu Coast) have not been taken into account. According to Song et al. (2013), Tao et al. (2011, 2018), Wang, Gao, et al. (2012), and Zhang and Chen (2011), large-scale human activities can modify the tidal wave systems and sediment transport patterns, hence have effects on the geomorphic development of the RSRs. The fact that these details concerning the hydrodynamic forcing and sediment transport processes can be ignored for simulating the formation of the RSRs and for reproducing their major characteristics reveals that the presented modeling has captured the major controlling factors for the development of the RSRs.
5. Main tidal constituents other than $M_2$ are not incorporated. However, the rms velocities of these constituents, such as $S_2$, $N_2$ and $K_1$, are comparable to that of the $M_2$ constituents. Therefore, the combination of these constituents can result in considerable spring-neap cyclic variability and more complicated spatial patterns of the current fields, which can affect the morphodynamics of the RSRs. These aspects require future research.

The neglected factors and processes also imply that not all the details of the morphology of the RSRs can be reproduced by the model. Albeit the simplified nature, by investigating the key parameters that affect the propagation of tidal wave systems and associated currents, as well as sediment supply, the model can capture the main features of the RSRs and provide insights into the mechanisms underlying the formation of the RSRs.

## 6. Conclusions

An open source numerical model (Delft3D) is employed to investigate the morphodynamics of the large-scale RSRs of the southern Yellow Sea off the Jiangsu Coast, China. The computational domain is schematically fan-shaped, and all the runs start from a smooth sloped bathymetry. Close-to-reality sand ridge patterns can be modeled with the configurations consistent with the current tidal regime of the RSRs. The numerical results directly demonstrate that the formation and the maintenance of the current morphology of the RSRs are governed by the specific tidal regime over the southern Yellow Sea. Such tidal regime is determined by the eastern coastline of China (e.g., the reflection of Shandong Peninsula) as well as latitudinal effects (i.e., the Coriolis force) of the RSRs. Deviation in the location of the amphidromic point can reduce the convergence of the tidal system waves to the central area of the RSRs, such that the development of the sand ridges is limited. The asymmetric spatial patterns of the RSRs characterized by larger northern sand ridges than the southern ones are promoted by the progressive tidal wave system and associated currents while are restricted by the rotational ones. The seaward extension of elongated sand ridges is subject to sediment supply. Insufficient sediment supply to the southern RSRs is another reason that the southern sand ridges are smaller than the northern ones in the RSRs. Overall, this study demonstrates that there is a delicate condition primarily represented by the particular currents governed by the tidal wave system and the sediment supply that are essential to shape the unique large-scale RSRs in the Southern Yellow Sea, which is different from other types of sand ridge systems around the world.

**Acknowledgments**
This study is supported by the National Natural Science Foundation of China (51620105005, 41606104, and 51739005), the National Key Research and Development Program of China (2018YFC0407501), and the Natural Science Foundation of Jiangsu Province (BK20160862). The open source code for Delft3D can be downloaded through their website (https://oss.deltares.nl/web/delft3d/). The bathymetric data used in the present study can be downloaded from GEBCO's gridded bathymetric data sets through their website (https://www.gebco.net/data_and_products/gridded_bathymetry_data/). The amplitudes and phases of the $M_2$ constituent used in the present study were extracted from a well-calibrated present-day tidal wave model that covers the Yellow Sea and East China Sea (Zhang et al., 1999, https://doi.org/10.1007/BF02878492). We highly appreciate three anonymous reviewers and the editors for their constructive comments.

## References

Bagnold, R. A. (1966). An approach to the sediment transport problem from general physics (USGS Professional Paper 422-I). Washington, DC: United States Government Printing Office.

Belderson, R. H., Johnson, M. A., & Kenyon, N. H. (1982). Bedforms. In A. H. Stride (Ed.), *Offshore tidal sands: Processes and deposits* (pp. 22–57). London: Chapman and Hall.

Blondeaux, P., De Swart, H. E., & Vittori, G. (2009). Long bed waves in tidal seas: An idealized model. *Journal of Fluid Mechanics*, *636*, 485–495. https://doi.org/10.1017/S0022112009990887

Calvete, D., De Swart, H. E., & Falqués, A. (2002). Effect of depth-dependent wave stirring on the final amplitude of shoreface-connected sand ridges. *Continental Shelf Research*, *22*(18-19), 2763–2776. https://doi.org/10.1016/S0278-4343(02)00125-5

Calvete, D., Falqués, A., De Swart, H. E., & Walgreen, M. (2001). Modelling the formation of shoreface-connected sand ridges on storm-dominated inner shelves. *Journal of Fluid Mechanics*, *441*, 169–193. https://doi.org/10.1017/S0022112001004815

Caston, G. F. (1981). Potential gain and loss of sand by some sand banks in the Southern Bight of the North Sea. *Marine Geology*, *41*(3-4), 239–250. https://doi.org/10.1016/0025-3227(81)90083-9

Collins, M. B., Shimwell, S. J., Gao, S., Powell, H., Hewitson, C., & Taylor, J. A. (1995). Water and sediment movement in the vicinity of linear sandbanks: The Norfolk Banks, southern North Sea. *Marine Geology*, *123*(3-4), 125–142. https://doi.org/10.1016/0025-3227(95)00010-V

Dastgheib, A., Roelvink, J. A., & Wang, Z. B. (2008). Long-term process-based morphological modeling of the Marsdiep Tidal Basin. *Marine Geology*, *256*(1-4), 90–100. https://doi.org/10.1016/j.margeo.2008.10.003

De Swart, H. E., Walgreen, M., Calvete, D., & Vis-Star, N. C. (2008). Nonlinear modelling of shoreface-connected ridges: Impact of grain sorting and interventions. *Coastal Engineering*, *55*(7-8), 642–656. https://doi.org/10.1016/j.coastaleng.2007.11.007

De Vriend, H. J. (1990). Morphological processes in shallow tidal seas. In R. T. Cheng (Ed.), *Residual currents and long-term transport, Coastal and Estuarine Studies* (Vol. 38, pp. 276–301). Washington, DC: American Geophysical Union. https://doi.org/10.1029/CE038p0276

Dissanayake, D. M. P. K., Roelvink, J. A., & Van der Wegen, M. (2009). Modelled channel patterns in a schematized tidal inlet. *Coastal Engineering*, *56*(11-12), 1069–1083. https://doi.org/10.1016/j.coastaleng.2009.08.008

Du, J., Shi, B., Li, J., & Wang, Y. P. (2018). Muddy coast off Jiangsu, China: Physical, ecological, and anthropogenic processes. In X. H. Wang (Ed.), *Sediment dynamics of Chinese muddy coasts and estuaries: Physics, biology, and their interactions* (pp. 25–49). San Diego, CA: Academic Press.

Du, J., & Wang, Y. P. (2014). Evolution simulation of radial sand ridges in the southern Yellow Sea (in Chinese with English abstract). *Journal of Nanjing University*, *50*(5), 636–645. https://doi.org/10.13232/j.cnki.jnju.2014.05.012

Dyer, K. R., & Huntley, D. A. (1999). The origin, classification and modelling of sand banks and ridges. *Continental Shelf Research*, *19*(10), 1285–1330. https://doi.org/10.1016/S0278-4343(99)00028-X

Engelund, F., & Hansen, E. (1967). *A monograph on sediment transport in alluvial streams (Technical Report)*. Copenhagen, Denmark: Teknisk Forlag.

Gao, S. (2013). Holocene shelf-coastal sedimentary systems associated with the Changjiang River: An overview. *Acta Oceanologica Sinica*, *32*(12), 4–12. https://doi.org/10.1007/s13131-013-0390-5

Gao, S., & Collins, M. B. (2014). Holocene sedimentary systems on continental shelves. *Marine Geology*, *352*, 268–294. https://doi.org/10.1016/j.margeo.2014.03.021

Garnier, R., Calvete, D., Falqués, A., & Caballeria, M. (2006). Generation and nonlinear evolution of shore-oblique/transverse sand bars. *Journal of Fluid Mechanics*, *567*, 327–360. https://doi.org/10.1017/S0022112006002126

Giosan, L., Donnelly, J. P., Vespremeanu, E., Bhattacharya, J. P., Olariu, C., & Buonaiuto, F. S. (2005). River delta morphodynamics: Examples from the Danube Delta. *Society for Sedimentary Geology, Special Publications of SEPM*, *83*, 393–411. https://doi.org/10.2110/pec.05.83.0393

Harris, P. T. (1988). Large-scale bedforms as indicators of mutually evasive sand transport and the sequential infilling of wide-mouthed estuaries. *Sedimentary Geology*, *57*(3-4), 273–298. https://doi.org/10.1016/0037-0738(88)90034-6

Hibma, A., Schuttelaars, H. M., & De Vriend, H. J. (2004). Initial formation and long-term evolution of channel-shoal patterns. *Continental Shelf Research*, *24*(15), 1637–1650. https://doi.org/10.1016/j.csr.2004.05.003

Hibma, A., Schuttelaars, H. M., & Wang, Z. B. (2003). Comparison of longitudinal equilibrium profiles of estuaries in idealized and process-based models. *Ocean Dynamic*, *53*(3), 252–269. https://doi.org/10.1007/s10236-003-0046-7

Houbolt, J. J. H. C. (1968). Recent sediments in the Southern Bight of the North Sea. *Geologie en Mijnbouw*, *47*(4), 245–273.

Hulscher, S. J. M. H., De Swart, H. E., & De Vriend, H. J. (1993). The generation of offshore tidal sand banks and sand waves. *Continental Shelf Research*, *13*(11), 1183–1204. https://doi.org/10.1016/0278-4343(93)90048-3

Huthnance, J. M. (1982a). On one mechanism forming linear sand banks. *Estuarine, Coastal and Shelf Science*, *14*(1), 79–99. https://doi.org/10.1016/S0302-3524(82)80068-6

Huthnance, J. M. (1982b). On the formation of sand banks of finite extent. *Estuarine, Coastal and Shelf Science*, *15*(3), 277–299. https://doi.org/10.1016/0272-7714(82)90064-6

Lee, H. J., & Chough, S. K. (1989). Sediment distribution, dispersal and budget in the Yellow Sea. *Marine Geology*, *87*(2-4), 195–205. https://doi.org/10.1016/0025-3227(89)90061-3

Lesser, G. R., Roelvink, J. A., Van Kester, J. A. T. M., & Stelling, G. S. (2004). Development and validation of a three-dimensional morphological model. *Coastal Engineering*, *51*(8-9), 883–915. https://doi.org/10.1016/j.coastaleng.2004.07.014

Li, C. X., Zhang, J. Q., Fan, D. D., & Deng, B. (2001). Holocene regression and the tidal radial sand ridge system formation in the Jiangsu coastal zone, east China. *Marine Geology*, *173*(1-4), 97–120. https://doi.org/10.1016/S0025-3227(00)00169-9

Liu, T., Shi, X., Li, C., & Yang, G. (2012). The reverse sediment transport trend between abandoned Huanghe River (Yellow River) Delta and radial sand ridges along Jiangsu coastline of China—An evidence from grain size analysis. *Acta Oceanologica Sinica*, *31*(6), 83–91. https://doi.org/10.1007/s13131-012-0255-3

Liu, Z., Huang, Y., & Zhang, Q. (1989). Tidal current ridges in the southwestern Yellow Sea. *Journal of Sedimentary Petrology*, *59*(3), 432–437. https://doi.org/10.1306/212F8FB7-2B24-11D7-8648000102C1865D

Liu, Z., & Xia, D. (1985). A preliminary study of tidal current ridges. *Chinese Journal of Oceanology and Limnology*, *3*(1), 118–133. https://doi.org/10.1007/BF02852909

Marciano, R., Wang, Z. B., Hibma, A., De Vriend, H. J., & Defina, A. (2005). Modeling of channel patterns in short tidal basins. *Journal of Geophysical Research*, *110*, F01001. https://doi.org/10.1029/2003JF000092

McBride, R. A., & Moslow, T. F. (1991). Origin, evolution, and distribution of shoreface sand ridges, Atlantic inner shelf, U.S.A. *Marine Geology*, *97*(1-2), 57–85. https://doi.org/10.1016/0025-3227(91)90019-Z

Milliman, J. D., Li, F., Zhao, Y., Zheng, T., & Limeburner, R. (1986). Suspended matter regime in the Yellow Sea. *Progress in Oceanography*, *17*(3-4), 215–227. https://doi.org/10.1016/0079-6611(86)90045-5

Milliman, J. D., & Meade, R. H. (1983). World-wide delivery of river sediment to the oceans. *The Journal of Geology*, *91*(1), 1–21. https://doi.org/10.1086/628741

Nnafie, A., De Swart, H. E., Calvete, D., & Garnier, R. (2014). Effects of sea level rise on the formation and drowning of shoreface-connected sand ridges, a model study. *Continental Shelf Research*, *80*, 32–48. https://doi.org/10.1016/j.csr.2014.02.017

Off, T. (1963). Rhythmic linear sand bodies caused by tidal currents. *Bulletin of the American Association of Petroleum Geologists*, *46*(2), 324–341. https://doi.org/10.1306/BC7437D5-16BE-11D7-8645000102C1865D

Pattiaratchi, C., & Collins, M. (1987). Mechanisms for linear sandbank formation and maintenance in relation to dynamical oceanographic observations. *Progress in Oceanography*, *19*(2), 117–176. https://doi.org/10.1016/0079-6611(87)90006-1

Qian, X., Chen, Y., Zhang, C., Pan, Y., & Das, H. (2015). Radial tidal current field in a semi-enclosed rectangular basin: Formation and evolution. *Chinese Journal of Oceanology and Limnology*, *33*(4), 1085–1099. https://doi.org/10.1007/s00343-015-4220-9

Ranasinghe, R., Swinkels, C., Luijendijk, A., Roelvink, D., Bosboom, J., Stive, M., & Walstra, D. (2011). Morphodynamic upscaling with the MORFAC approach: Dependencies and sensitivities. *Coastal Engineering*, *58*(8), 806–811. https://doi.org/10.1016/j.coastaleng.2011.03.010

Ren, M. E. (Ed.) (1986). *Comprehensive investigation of the coastal zone and tidal land resources of Jiangsu Province* (in Chinese). Beijing: China Ocean Press.

Ren, M. E., Zhang, R., & Yang, J. (1985). Effect of Typhoon No.8114 on coastal morphology and sedimentation of Jiangsu Province, People's Republic of China. *Journal of Coastal Research*, *1*(1), 21–28.

Reynaud, J., Tessier, B., Berné, S., Chamley, H., & Debatist, M. (1999). Tide and wave dynamics on a sand bank from the deep shelf of the Western Channel approaches. *Marine Geology*, *161*(2-4), 339–359. https://doi.org/10.1016/S0025-3227(99)00033-X

Rodríguez-Iturbe, I., Rinaldo, A., Rigon, R., Bras, R. L., Marani, A., & Ijjász-Vásquez, E. (1992). Energy dissipation, runoff production, and the three-dimensional structure of river basins. *Water Resources Research*, *28*(4), 1095–1103. https://doi.org/10.1029/91WR03034

Roelvink, J. A. (2006). Coastal morphodynamic evolution techniques. *Coastal Engineering*, *53*(2-3), 277–287. https://doi.org/10.1016/j.coastaleng.2005.10.015

Saito, Y., & Yang, Z. (1994). Historical change of the Huanghe (Yellow River) and its impact on the sediment budget of the East China Sea. In S. Tsunogai, K. Iseki, I. Koike, & T. Oba (Eds.), *Global fluxes of carbon and its related substances in the coastal sea-ocean-atmosphere system* (pp. 7–12). Yokohama: M & J International.

Schramkowski, G. P., & De Swart, H. E. (2002). Morphodynamic equilibrium in straight tidal channels: Combined effects of the Coriolis force and external overtides. *Journal of Geophysical Research*, *107*(C12), 3227. https://doi.org/10.1029/2000JC000693

Song, D., Wang, X. H., Zhu, X., & Bao, X. (2013). Modeling studies of the far-field effects of tidal flat reclamation on tidal dynamics in the East China Seas. *Estuarine, Coastal and Shelf Science*, *133*, 147–160. https://doi.org/10.1016/j.ecss.2013.08.023

Soulsby, R. (1997). *Dynamics of marine sands: A manual for practical applications*. London: Thomas Telford.

Stride, A. H. (1982). *Offshore tidal sands: Processes and deposits*. London: Chapman and Hall. https://doi.org/10.1007/978-94-009-5726-8

Swift, D. J. P. (1975). Tidal sand ridges and shoal-retreat massifs. *Marine Geology*, *18*(3), 105–133. https://doi.org/10.1016/0025-3227(75)90007-9

Tao, J., Xu, F., Yao, P., Zhou, Z., & Zhang, C. (2018). The variations of sediment transport patterns in the radial sand ridges along the Jiangsu coast, China over the last 30 years. *Journal of Coastal Research*, *85*(SI), 216–220. https://doi.org/10.2112/SI85-044.1

Tao, J. F., Yang, T., Xu, F., & Yao, J. (2011). Effect of large scale tidal flat reclamation on hydrodynamic circulation in Jiangsu coastal areas. In J. H.-W. Lee & C.-O. Ng (Eds.), *Asian and Pacific Coasts 2011* (pp. 662–669). Singapore: World Scientific. https://doi.org/10.1142/9789814366489_0077

Tao, J. F., Zhang, C. K., Yao, J., & Gong, Z. (2009). Numerical simulation of tides and tidal currents in Jiangsu offshore areas, China. Paper presented at the 19th International Offshore and Polar Engineering Conference, Osaka, Japan, 1243-1247.

Trowbridge, J. H. (1995). A mechanism for the formation and maintenance of shore-oblique sand ridges on storm-dominated shelves. *Journal of Geophysical Research*, *100*(C8), 16,071–16,086. https://doi.org/10.1029/95JC01589

Uehara, K., & Saito, Y. (2003). Late Quaternary evolution of the Yellow/East China Sea tidal regime and its impacts on sediments dispersal and seafloor morphology. *Sedimentary Geology*, *162*(1-2), 25–38. https://doi.org/10.1016/S0037-0738(03)00234-3

Uehara, K., Saito, Y., & Hori, K. (2002). Paleotidal regime in the Changjiang (Yangtze) Estuary, the East China Sea, and the Yellow Sea at 6 ka and 10 ka estimated from a numerical model. *Marine Geology*, *183*(1-4), 179–192. https://doi.org/10.1016/S0025-3227(01)00255-9

Van de Meene, J. W. H., & Van Rijn, L. C. (2000a). The shoreface-connected ridges along the central Dutch coast—Part 1: Field observations. *Continental Shelf Research*, *20*(17), 2295–2323. https://doi.org/10.1016/S0278-4343(00)00048-0

Van de Meene, J. W. H., & Van Rijn, L. C. (2000b). The shoreface-connected ridges along the central Dutch coast—Part 2: Morphological modelling. *Continental Shelf Research*, *20*(17), 2325–2345. https://doi.org/10.1016/S0278-4343(00)00049-2

Van der Wegen, M., & Roelvink, J. A. (2008). Long-term morphodynamic evolution of a tidal embayment using a two-dimensional, process-based model. *Journal of Geophysical Research*, *113*, C03016. https://doi.org/10.1029/2006JC003983

Van der Wegen, M., Wang, Z. B., Savenije, H. H. G., & Roelvink, J. A. (2008). Long-term morphodynamic evolution and energy dissipation in a coastal plain, tidal embayment. *Journal of Geophysical Research*, *113*, F03001. https://doi.org/10.1029/2007JF000898

Van Leeuwen, S. M., & De Swart, H. E. (2002). Intermediate modelling of tidal inlet systems: Spatial asymmetries in flow and mean sediment transport. *Continental Shelf Research*, *22*(11-13), 1795–1810. https://doi.org/10.1016/S0278-4343(02)00038-9

Van Maanen, B., Coco, G., & Bryan, K. R. (2013). Modelling the effects of tidal range and initial bathymetry on the morphological evolution of tidal embayments. *Geomorphology*, *191*, 23–34. https://doi.org/10.1016/j.geomorph.2013.02.023

Van Rijn, L. C. (1993). *Principles of sediment transport in rivers, estuaries and coastal seas*. Amsterdam: Aqua Publications.

Vis-Star, N. C., De Swart, H. E., & Calvete, D. (2009). Effect of wave–bedform feedbacks on the formation of, and grain sorting over shoreface-connected sand ridges. *Ocean Dynamics*, *59*(5), 731–749. https://doi.org/10.1007/s10236-009-0210-9

Walgreen, M., Calvete, D., & De Swart, H. E. (2002). Growth of large-scale bed forms due to storm-driven and tidal currents: A model approach. *Continental Shelf Research*, *22*(18-19), 2777–2793. https://doi.org/10.1016/S0278-4343(02)00126-7

Wang, X., & Ke, X. (1997). Grain-size characteristics of the extant tidal flat sediments along the Jiangsu coast, China. *Sedimentary Geology*, *112*(1-2), 105–122. https://doi.org/10.1016/S0037-0738(97)00026-2

Wang, Y., Zhang, Y., Zou, X., Zhu, D., & Piper, D. (2012). The sand ridge field of the South Yellow Sea: Origin by river-sea interaction. *Marine Geology*, *291-294*, 132–146. https://doi.org/10.1016/j.margeo.2011.01.001

Wang, Y., Zhu, D., You, K., Pan, S., Zhu, X., Zou, X., & Zhang, Y. (1999). Evolution of radiative sand ridge field of the South Yellow Sea and its sedimentary characteristics. *Science in China, Series D: Earth Sciences*, *42*(1), 97–112. https://doi.org/10.1007/BF02878503

Wang, Y. P., Gao, S., Jia, J., Thompson, C. E. L., Gao, J., & Yang, Y. (2012). Sediment transport over an accretional intertidal flat with influences of reclamation, Jiangsu coast, China. *Marine Geology*, *291-294*, 147–161. https://doi.org/10.1016/j.margeo.2011.01.004

Wang, Z. B., Louters, T., & De Vriend, H. J. (1995). Morphodynamic modelling for a tidal inlet in the Wadden Sea. *Marine Geology*, *126*(1-4), 289–300. https://doi.org/10.1016/0025-3227(95)00083-B

Winterwerp, J. C., & Wang, Z. B. (2013). Man-induced regime shifts in small estuaries—I: Theory. *Ocean Dynamics*, *63*(11-12), 1279–1292. https://doi.org/10.1007/s10236-013-0662-9

Winterwerp, J. C., Wang, Z. B., Van Braeckel, A., Van Holland, G., & Kösters, F. (2013). Man-induced regime shifts in small estuaries—II: A comparison of rivers. *Ocean Dynamics*, *63*(11-12), 1293–1306. https://doi.org/10.1007/s10236-013-0663-8

Xing, F., Wang, Y. P., & Wang, H. V. (2012). Tidal hydrodynamics and fine-grained sediment transport on the radial sand ridge system in the southern Yellow Sea. *Marine Geology*, *291-294*, 192–210. https://doi.org/10.1016/j.margeo.2011.06.006

Xiong, J., Wang, X. H., Wang, Y. P., Chen, J., Shi, B., Gao, J., et al. (2017). Mechanisms of maintaining high suspended sediment concentration over tide-dominated offshore shoals in the southern Yellow Sea. *Estuarine, Coastal and Shelf Science*, *191*, 221–233. https://doi.org/10.1016/j.ecss.2017.04.023

Xu, F., Tao, J., Zhou, Z., Coco, G., & Zhang, C. (2016). Mechanisms underlying the regional morphological differences between the northern and southern radial sand ridges along the Jiangsu Coast, China. *Marine Geology*, *371*, 1–17. https://doi.org/10.1016/j.margeo.2015.10.019

Yang, C. S. (1989). Active, moribund and buried tidal sand ridges in the East China Sea and the Southern Yellow Sea. *Marine Geology*, *88*(1-2), 97–116. https://doi.org/10.1016/0025-3227(89)90007-8

Zhang, C., Zhang, D., Zhang, J., & Wang, Z. (1999). Tidal current-induced formation—storm-induced change—tidal current-induced recovery—Interpretation of depositional dynamics of formation and evolution of radial sand ridges on the Yellow Sea seafloor. *Science in China, Series D: Earth Sciences*, *42*(1), 1–12. https://doi.org/10.1007/BF02878492

Zhang, C. K. (Ed.) (2012). *Comprehensive investigation and assessment report of Jiangsu offshore* (in Chinese). Beijing: China Science Press.

Zhang, C. K., & Chen, J. (2011). Master plan of tidal flat reclamation along Jiangsu coastal zone. In J. H.-W. Lee & C.-O. Ng (Eds.), *Asian and Pacific coasts 2011* (pp. 139–146). Singapore: World Scientific. https://doi.org/10.1142/9789814366489_0016

Zhang, R. S. (1984). Land-forming history of the Huanghe River delta and coastal plain of north Jiangsu (in Chinese with English abstract). *Acta Geographica Sinica*, *39*(2), 173–184.

Zhou, L., Liu, J., Saito, Y., Zhang, Z., Chu, H., & Hu, G. (2014). Coastal erosion as a major sediment supplier to continental shelves: Example from the abandoned Old Huanghe (Yellow River) delta. *Continental Shelf Research*, *82*, 43–59. https://doi.org/10.1016/j.csr.2014.03.015

Zhou, Z., Coco, G., Jiménez, M., Olabarrieta, M., Van der Wegen, M., & Townend, I. (2014). Morphodynamics of river-influenced back-barrier tidal basins: The role of landscape and hydrodynamic settings. *Water Resources Research*, *50*, 9514–9535. https://doi.org/10.1002/2014WR015891

Zhou, Z., Coco, G., Townend, I., Olabarrieta, M., van der Wegen, M., Gong, Z., et al. (2017). Is "morphodynamic equilibrium" an oxymoron? *Earth-Science Reviews*, *165*, 257–267. https://doi.org/10.1016/j.earscirev.2016.12.002

Zhou, Z., Olabarrieta, M., Stefanon, L., D'Alpaos, A., Carnlello, L., & Coco, G. (2014). A comparative study of physical and numerical modeling of tidal network ontogeny. *Journal of Geophysical Research: Earth Surface*, *119*, 892–912. https://doi.org/10.1002/2014JF003092

Zhu, Y., & Chang, R. (2001). On the relationships between the radial tidal current field and the radial sand ridges in the southern Yellow Sea: A numerical simulation. *Geo-Marine Letters*, *21*(2), 59–65. https://doi.org/10.1007/s003670100073

Zhu, Y., & Chen, Q. (2005). On the origin of the radial sand ridges in the Southern Yellow Sea: Results from the modeling of the paleoradial tidal current fields off the Paleo-Yangtze River Estuary and Northern Jiangsu Coast. *Journal of Coastal Research*, *216*(6), 1245–1256. https://doi.org/10.2112/02-0054.1